

Quartet states in two-electron quantum dots in bilayer graphene

Angelika Knothe¹ and Vladimir Fal'ko^{1,2,3}

¹*National Graphene Institute, University of Manchester, Manchester M13 9PL, United Kingdom*

²*Department of Physics and Astronomy, University of Manchester, Oxford Road, Manchester, M13 9PL, United Kingdom and*

³*Henry Royce Institute for Advanced Materials, University of Manchester, Manchester, M13 9PL, United Kingdom*

(Dated: March 2, 2020)

Trapping electrons in quantum dots and controlling their collective quantum states is crucial for converting semiconductor structures into bits of quantum information processing. Here, we study single- and two-particle states in quantum dots formed in gapped bilayer graphene (BLG), where the electron's valley states appear in pair with their spin quantum number and we analyse spin- and valley-singlet and triplet states for various BLG and dot parameters, as well as two-particle interaction strength and external magnetic field.

Few-electron quantum dots (QD) were extensively investigated in various semiconductors (Si^{1,2}, GaAs/AlGaAs heterostructures³⁻⁵, varieties of type III - IV semiconductors⁶⁻⁸), where the understanding of the QD's ground state (GS), excitations, and addition spectra led to the suggestions⁹ for their use as solid state qubits¹⁰⁻¹⁴. The extensive studies of few-electron states in QDs made of conventional gap-full semiconductors have already resulted in a complete understanding of their GS and excitation properties. Here, we study two-electron states (2ES) in QDs based on a semimetal with a non-trivial multi-valley band structure, namely, bilayer graphene (BLG). Due to the features of the BLG electronic spectrum, the theoretical description of 2ES in BLG QDs lacks the elegant exact solutions developed for two electrons with parabolic dispersion^{15,16}, and, here, we develop a combined analytical and computational approach to describe their low-energy spectra.

To create QDs in BLG, one needs to open an interlayer asymmetry gap¹⁷ in this, otherwise, gapless semiconductor and, then, to confine electrons using a combination of top and bottom gates¹⁸⁻²². Upon opening a gap, the spectrum of electrons of both, the conduction, and the valence band edges acquire a strongly non-parabolic dispersion²³⁻²⁵, which even has a slightly inverted form featuring three shallow minivalleys around both, K^+ and K^- , valleys. This comes on top of graphene's valley (T) and spin (S) quantum numbers. The flat band edge promotes the formation of different spin and valley multiplets for the low-energy two-particle QD states, illustrated in Fig. 1. Typically, we find that the GS is a multiplet that includes simultaneous spin and valley singlets and triplets, prescribed by the electron-electron exchange interaction. Depending on the dot size and the interlayer asymmetry gap, the first excited state may belong to a different spin/valley multiplet, with fine energy splittings determined by inter- and intra-valley interactions between electrons. Additionally, one can use an external magnetic field to tune the valley splitting²⁵⁻²⁷ due to the valley-dependent topological magnetic moment of the electrons²⁸.

Below, we describe interacting electrons in a BLG QD

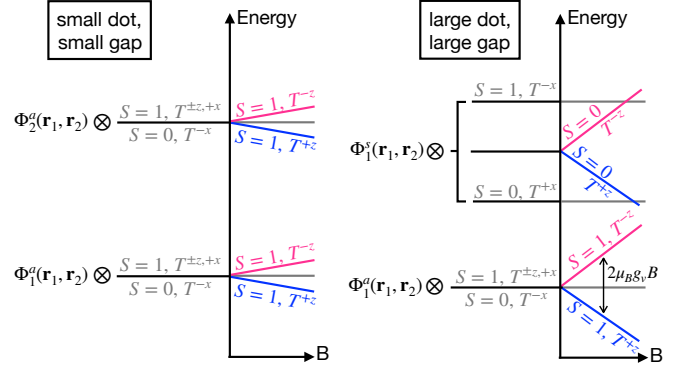


FIG. 1. Level schemes for two strongly interacting electrons confined in a QD in BLG with a weak gap (left), or a strong gap (right): a two-particle state where the orbital part of the wave function is antisymmetric, Φ^a , minimizes the charging energy and entails the GS. Higher-energy states can be orbitally symmetric or antisymmetric. Short-range interactions determine splittings between spin singlets ($S = 0$) and triplets ($S = 1$), and valley singlets (T^{-x}) and triplets ($T^{\pm z, +x}$). Valley polarized states are split linearly in a weak magnetic field²⁸ according to their valley g-factor, g_v .

using a Hamiltonian,

$$\hat{H} = \hat{H}^0 + \hat{V} + \hat{U}. \quad (1)$$

Here, \hat{H}^0 , is a single-particle part (specified below) taking into account the BLG dispersion and a smooth electrostatic confinement. The operator \hat{V} , acts on the orbital part, $\Phi_\alpha(\mathbf{r}_1, \mathbf{r}_2)$, of the two-particle wave function,

$$V_{\alpha, \beta} = \iint d\mathbf{r}_1 d\mathbf{r}_2 \Phi_\alpha^*(\mathbf{r}_1, \mathbf{r}_2) V(\mathbf{r}_1 - \mathbf{r}_2) \Phi_\beta(\mathbf{r}_1, \mathbf{r}_2), \quad (2)$$

and takes into account the 2D screened Coulomb interaction in a weakly gapped BLG²⁹. Its Fourier representation, $V(\mathbf{q}) = \frac{e^2}{4\pi\epsilon_0\epsilon} \frac{2\pi}{q(1+qR_s)}$ (where ϵ_0 is the vacuum permittivity and ϵ is the dielectric constant of the encapsulating substrate material, such as hBN), takes into account the polarizability of gapped BLG²⁹, with $\kappa^2 = 2me^2/(4\pi\epsilon_0\epsilon\hbar\sqrt{\Delta})^2$ (m being the effective mass). It results in a Keldysh-like potential³⁰⁻³²,

$V(r < R_*) \propto \frac{e^2}{\epsilon R_*} \ln(r/R_*)$, and $V(r \gg R_*) \propto \frac{e^2}{\epsilon r}$ (with $R_* = \sqrt{32\hbar\kappa}/\sqrt{\Delta}$). The last term in Eq. (1) takes into account short-range (lattice-constant-scale) electron-electron interactions^{33–35},

$$\hat{U} = \hat{W} \otimes \begin{pmatrix} g_{zz} & 0 & 0 & 0 \\ 0 & g_{zz} & 4g_{\perp} & 0 \\ 0 & 4g_{\perp} & g_{zz} & 0 \\ 0 & 0 & 0 & g_{zz} \end{pmatrix},$$

$$W_{\alpha,\beta} = \frac{1}{2} \int d\mathbf{r} \Phi_{\alpha}^*(\mathbf{r}, \mathbf{r}) \Phi_{\beta}(\mathbf{r}, \mathbf{r}), \quad (3)$$

which is written in the basis of valley Bloch states, $\{K_1^+ K_2^+, K_1^+ K_2^-, K_1^- K_2^+, K_1^- K_2^-\}$, of the two electrons ($\xi = \pm 1$ is the valley index). The coupling parameters g_{zz} (intra-valley) and g_{\perp} (inter-valley short-range interaction) and the role they play in splitting the low-energy multiplets will be discussed later in the text.

For a BLG QD, formed with the help of electrostatic split gates^{19,36,37}, we employ a circularly symmetric potential, $U(\mathbf{r})$, and a gap profile, $\Delta(\mathbf{r})$, which enter in the single-electron four-band Hamiltonian^{38,39},

$$\hat{H}_{\pm}^0 = \begin{pmatrix} U \mp \frac{1}{2}\Delta & \pm v_3\pi & 0 & \pm v\pi^{\dagger} \\ \pm v_3\pi^{\dagger} & U \pm \frac{1}{2}\Delta & \pm v\pi & 0 \\ 0 & \pm v\pi^{\dagger} & U \pm \frac{1}{2}\Delta & \gamma_1 \\ \pm v\pi & 0 & \gamma_1 & U \mp \frac{1}{2}\Delta \end{pmatrix},$$

$$U(\mathbf{r}) = \frac{U_0}{\cosh \frac{r}{L}}, \quad \Delta(\mathbf{r}) = \Delta_0 - \frac{0.3\Delta_0}{\cosh \frac{r}{L}}. \quad (4)$$

with $\mathbf{r} = (x, y)$, $r = |\mathbf{r}|$, momenta $\pi = p_x + ip_y$, $\pi^{\dagger} = p_x - ip_y$ (where $\mathbf{p} = -i\hbar\nabla$), velocities $v = 1.02 * 10^6$ m/s and $v_3 \approx 0.12v$, and energy $\gamma_1 \approx 0.38$ eV. This Hamiltonian is written for the Bloch function components $\psi_{K^+} = (\psi_A, \psi_{B'}, \psi_{A'}, \psi_B)$ in valley K^+ , and $\psi_{K^-} = (\psi_{B'}, \psi_A, \psi_B, \psi_{A'})$ in valley K^- , with electron's amplitudes on the BLG sublattices A and B in the top, and A' and B' in the bottom layer. In the absence of confinement, Eq. (4) describes the low energy trigonally warped bands^{23–25} featuring three minivalleys around each K point (Fig. 2 inset).

To study the 2ES properties of the QD, we proceed as follows. First, we numerically diagonalize the Hamiltonian in Eq. (4) in a basis of localized states (SI section S1) and obtain the single-particle spectrum of the QD, $\Psi_n(\mathbf{r})$. Using those states, we construct a basis of symmetrized (s) or antisymmetrized (a) two-particle orbital wave functions,

$$\phi_{ij}^{s/a}(\mathbf{r}_1, \mathbf{r}_2) = \frac{1}{\sqrt{2}} [\Psi_i(\mathbf{r}_1)\Psi_j(\mathbf{r}_2) \pm \Psi_i(\mathbf{r}_2)\Psi_j(\mathbf{r}_1)], \quad (5)$$

and compute the matrix elements of the interaction operators \hat{V} and \hat{U} in Eq. (1). Diagonalizing the resulting matrix yields the QD 2ES energy spectrum, \mathfrak{E} , and wave functions, $\Phi^{s/a}(\mathbf{r}_1, \mathbf{r}_2) = \sum_{\alpha} \lambda_{\alpha}^{s/a} \phi_{\alpha}^{s/a}(\mathbf{r}_1, \mathbf{r}_2)$, $\alpha = ij$ (SI section S5). Note that for the symmetric states, we sum over $\alpha \in \{11, 12, \dots\}$, whereas for the antisymmetric

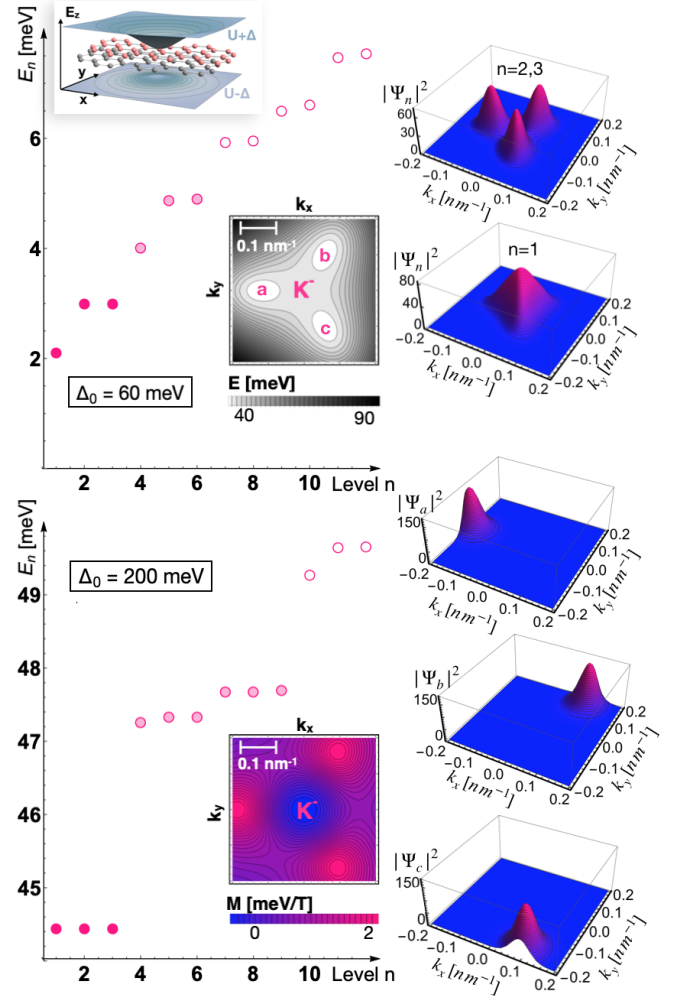


FIG. 2. Single-particle energy spectra for $U_0 = -20$ meV, $L = 80$ nm, and a small gap ($\Delta_0 = 60$ meV) or a large gap ($\Delta_0 = 200$ meV), demonstrating the change of multiplicity as the GS develops from a non-degenerate state to a threefold-degenerate state. Shadings of the dots indicate which levels are populated by a two-electron state: For no or weak interactions, only the lowest states are populated (dark circles). For stronger interaction, states are mixed and higher energy states are involved (light circles). The higher lying states remain unpopulated (empty circles). To the right, we show the probability distribution, $|\Psi_n|^2$, in valley K^- for the lowest levels $n = 1, 2, 3$ (small gap), or the states in the minivalleys $n = a, b, c$ (large gap). Insets: Electrostatic potential realizing the confinement; dispersion, E , of the first conduction band of gapped BLG with a gap of $\Delta = 70$ meV; corresponding orbital magnetic moment, M , around the K^- -valley.

states indices run over $\alpha \in \{12, 13, \dots\}$ (excluding mn combinations).

In Fig. 2, we illustrate single-particle spectra, E_n , for a dot with $U_0 = -20$ meV, $L = 80$ nm and different values of Δ_0 . Alongside this, we plot the probability distribution, $|\Psi_n(\mathbf{k})|^2$, (in valley K^-) for the lowest three levels. The trigonally warped mini-valley structure de-

termines C_3 rotational symmetry of the system, even for a circularly symmetric confinement potential. This symmetry breaking lifts the degeneracies of the usual Fock-Darwin levels^{40,41}, commonly used for describing the discrete electronic states of a QD in 2D electron gases under circular harmonic confinement (see SI section S2 and S3). For smaller dots in BLG with a smaller Δ_0 and stronger confinement, the Fourier transform of the wave function is squeezed towards the center of the K -valleys in momentum space (top left panel of Fig. 2). This suppresses the minivalley effect, leading to a non-degenerate GS, Ψ_1 , isolated from the rest of the spectrum by several meV. Higher states, Ψ_n with $n > 1$, come in approximate doublets. Upon increasing Δ_0 , the single-particle level structure evolves into clearly identifiable mini-valley triplets, as shown in Fig. 2 for $\Delta_0 = 200$ meV. For a large enough gap, the minivalleys are sufficiently developed and separated far enough in momentum space to represent a good quantum number. In this regime, all the single-particle levels are threefold degenerate (three minivalleys in each valley, the corresponding single-particle wave functions are shown in Fig. 2 in momentum space and in Fig. 3 in real space). For this reason, it is beneficial to identify the basis of minivalleys, which we label by a, b, c (and use below for the interpretation of the 2ES),

$$\begin{aligned}\Psi_a &= (\Psi_1 + \Psi_2 + \Psi_3)/\sqrt{3}, \\ \Psi_b &= (\Psi_1 + e^{-i\frac{2\pi}{3}}\Psi_2 + e^{i\frac{2\pi}{3}}\Psi_3)/\sqrt{3}, \\ \Psi_c &= (\Psi_1 + e^{i\frac{2\pi}{3}}\Psi_2 + e^{-i\frac{2\pi}{3}}\Psi_3)/\sqrt{3}.\end{aligned}\quad (6)$$

To mention, in SI section S4, we describe selection rules for optical transitions between these for both types of spectra shown in Fig. 2. Also, the states of gapped BLG carry a non-zero orbital magnetic moment, $M_z(\pm K) = \pm\mu_B g_v(\mathbf{k})$,^{42,43} which has opposite signs in the opposite valleys. It is convenient to characterise this quantity using a valley g-factor, g_v , that is small for the states exactly at the centre of the K^\pm valleys and reaches a magnitude of $g_v \sim 10^2$ at the mini-valley dispersion minima^{25,27}, (inset to Fig. 2). The valley dependence of $M_z(k)$ leads to the valley splitting, $2B_z\mu_B$ in an external magnetic field²⁸, which we take into account at the end of this analysis in relation to the fine structure of the 2ESs. An orbital magnetic moment implies some angular momentum, whose coupling to the orbital motion of an electron results in a small splitting of the higher QD levels, E_2 and E_3 (see SI section S2).

To find the spectra of two electron states in a dot we solve the eigenvalue equation,

$$\begin{aligned}\hat{H}\Phi &= \mathfrak{E}\Phi \Leftrightarrow \sum_{\beta=kl} [E_i\delta_{ik} + E_j\delta_{jl} + V_{\alpha,\beta}^{s/a} + \delta\mathfrak{E}_{\alpha,\beta}^{s/a}(\tau)]\lambda_\beta^{s/a} = \mathfrak{E}^{s/a}\lambda_\alpha^{s/a}, \quad \alpha = ij, \\ V_{\alpha,\beta}^{s/a} &= V_{ik,jl} \pm V_{il,jk}, \quad V_{ij,kl} = \iint d\mathbf{r}_1 d\mathbf{r}_2 \Psi_i^*(\mathbf{r}_1)\Psi_j(\mathbf{r}_1)V(\mathbf{r}_1 - \mathbf{r}_2)\Psi_k^*(\mathbf{r}_2)\Psi_l(\mathbf{r}_2), \\ \delta\mathfrak{E}_{\alpha,\beta}^s(T^{\pm z}) &= W_{\alpha,\beta} g_{zz}, \quad \delta\mathfrak{E}_{\alpha,\beta}^s(T^{\pm x}) = W_{\alpha,\beta}(g_{zz} \pm g_\perp), \quad \delta\mathfrak{E}^a \equiv 0, \\ W_{\alpha,\beta} &= \int d\mathbf{r}\Psi_i^*(\mathbf{r})\Psi_j^*(\mathbf{r})\Psi_k(\mathbf{r})\Psi_l(\mathbf{r}).\end{aligned}\quad (7)$$

In Eq. (7), we distinguish between the symmetric and antisymmetric combinations of single-particle orbitals, as introduced in Eq. (5), which is also related to the structure of multiplets, τ , involving valley degrees of freedom. "Valley triplet" states comprise the polarized states, $\tau = T^{\pm z}$ ($K_1^+K_2^+$ and $K_1^-K_2^-$), and the coherent combination, $\tau = T^{+x}$ ($[K_1^+K_2^- + K_1^-K_2^+]/\sqrt{2}$), and they are complemented by the "valley singlet", $\tau = T^{-x}$ ($[K_1^+K_2^- - K_1^-K_2^+]/\sqrt{2}$). These valley multiplets come on top of the conventional classification of spin-singlet and -triplet states²⁸.

Depending on the interaction strengths, various combinations of valley-/spin-singlets and -triplets appear as

the low-energy eigenstates of the Hamiltonian in Eq. (7). For sufficiently strong long-range interaction, \hat{V} , the GS will be an antisymmetric combination of orbitals, Φ^a , as favored by the exchange interaction. For weak long-range interactions (compared to the gaps in the noninteracting 2ES spectrum), orbitally symmetric GSs may occur, Φ^s , for which different valley states are shifted by $W_{\alpha,\beta} g_{zz}$ and split proportionally to $W_{\alpha,\beta} g_\perp$, according to Eq. (7).

To compare different interaction energies in Eq. (7), we estimate the valley splittings of the orbitally symmetric states, $\Phi^s(\mathbf{r}_1, \mathbf{r}_2)$. From the lowest single-particle wave functions, Ψ_1 , for $L = 80$ nm and a gap of $\Delta_0 = 60$ meV we calculate $W_{11,11} = 4.3 * 10^{-4}$ nm⁻².

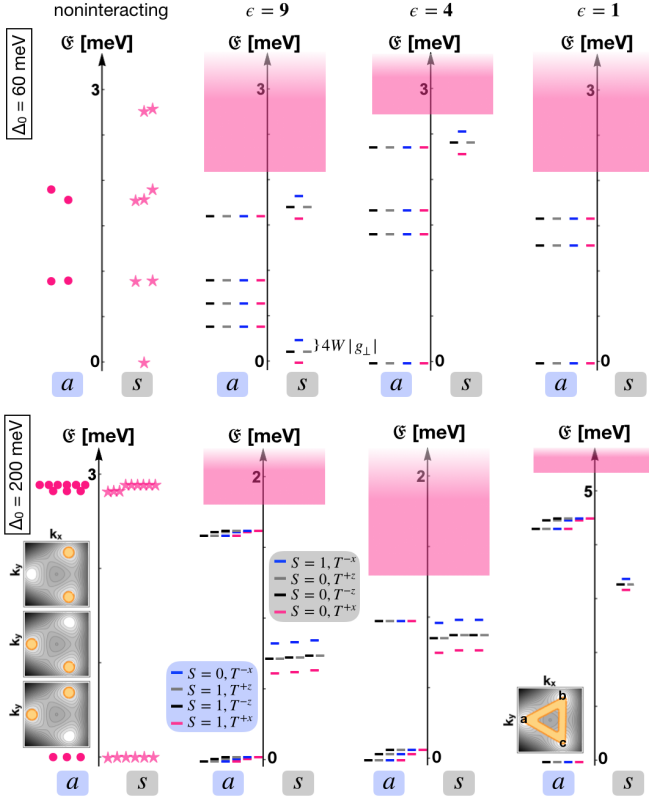


FIG. 3. Two-particle spectra for interacting electrons depending on the dielectric constant, ϵ , of the encapsulating medium in QDs in BLG with a small gap (top row, $\Delta_0=60$ meV) and a large gap (bottom row, $\Delta_0=200$ meV) computed in the subspace of the $N = 6$ or $N = 9$ lowest single-particle states $\Psi_n(\mathbf{r})$. For the noninteracting case, magenta dots (stars) represent the energies of antisymmetric (symmetric) orbital states, each four-fold degenerate in the spin and valley degree of freedom. For non-zero interactions, we identify the spin/valley configurations of the multiplets by lines of different color and indicate the onset of a continuum by a magenta bar. The case $\epsilon = 4$ (BLG encapsulated by hBN^{30,44}) corresponds to Fig. 1. Insets portray mini-valley-incoherent (noninteracting) or mini-valley-coherent (strongly interacting, $\epsilon = 1$) 2ESs.

For a rough estimate of numerical values for the couplings $g_{zz,\perp}$, we use the p_z -orbitals in the BLG Bloch states (SI section S6), and obtain $g_{zz} = 4.04/\epsilon_c$ eVnm², $g_{\perp} = -0.191/\epsilon_c$ eVnm², in accordance with previous estimations of the microscopic coupling parameters in monolayer and bilayer graphene^{45,46}, which likewise suggested $g_{zz} > 0, g_{\perp} < 0$ and $g_{zz} > |g_{\perp}|$. Here, $\epsilon_c \approx 2.65$, is the dielectric susceptibility of BLG⁴⁷. We estimate a shift of the orbitally symmetric states of $W_{11,11}$ $g_{zz} = 0.66$ meV, and a valley splitting of $4|W_{11,11} g_{\perp}| = 0.14$ meV. For $\Delta_0 = 200$ meV we obtain $W_{11,11} = 3.7 * 10^{-4}$ nm⁻², entailing $W_{11,11} g_{zz} = 0.56$ meV and $4|W g_{\perp}| = 0.11$ meV⁴⁸. Below, we will drop the indices for brevity, implying $W = W_{11,11}$.

Combining the latter estimates with the numerical

evaluation of the Coulomb matrix elements in Eq. (7), we calculate the spectra for the 2ES, such as those illustrated in Fig. 3 for several values of the dielectric constant ϵ of the encapsulated medium and for $\Delta_0 = 60$ meV and $\Delta_0 = 200$ meV (energies of the states are listed in SI section S7). We distinguish between the spectra of orbitally antisymmetric and orbitally symmetric states, and identify the splittings of valley multiplets.

In the absence of interactions ($\epsilon \rightarrow \infty$), 2ESs are exact combinations of the single-particle states as written in Eq. (5). In the case of a small gap, $\Delta_0 = 60$ meV, and $\epsilon = \infty$, the two-particle GS is the singly-degenerate state Φ_{11}^s (upper left panel in Fig. 3), since the single-particle GS, Ψ_1 , is non-degenerate and therefore $\mathfrak{E}_{11}^s < \mathfrak{E}_{12}^a = \mathfrak{E}_{13}^a$. This orbital composition of the GS is stable against a weak interaction ($\epsilon = 9$ in Fig. 3) where the electron repulsion is not sufficient to alter the orbital wave function. Hence, in the weakly interacting regime, the first orbital symmetric state, Φ_{11}^s , remains to be the basis for the GS and the corresponding spin and valley levels are shifted and split according to the short-range interaction part, $\delta\mathfrak{E}^s$, in Eq. (7). As the overall wavefunction should be antisymmetric, the resulting GS is a spin-singlet ($S = 0$) and a valley triplet (T^{+x}). This form of the QD GS resembles a singlet Cooper pair as in the superconducting phase discussed previously in BLG as a consequence of short-range interactions³⁴.

Conversely, if the gap is large enough for the gapped BLG mini-valleys to survive size quantization ($\Delta_0 = 200$ in Fig. 3), the noninteracting two-particle GS acquires an additional degeneracy. Orbitally symmetric and antisymmetric states can occur at equal energy, $\mathfrak{E}_{11}^s = \mathfrak{E}_{12}^s = \mathfrak{E}_{13}^s = \mathfrak{E}_{22}^s = \mathfrak{E}_{23}^s = \mathfrak{E}_{33}^s = \mathfrak{E}_{12}^a = \mathfrak{E}_{13}^a = \mathfrak{E}_{23}^a$, due to the three mini-valley states of the single-particle GSs, Ψ_1, Ψ_2 , and Ψ_3 (bottom left panel in Fig. 3). This latter degeneracy is conveniently exploited using the basis of minivalleys states Ψ_a, Ψ_b, Ψ_c (see Eq. (6)). Then, combinations of the orbitally asymmetric 2ESs, Φ_{ab}^a, Φ_{ac}^a , and Φ_{bc}^a , where each electron sits in its own mini-valley (shown as insets to the bottom left panel of Fig. 3), determine the three-fold degenerate GS of the system at zero or weak interactions:

$$\begin{aligned}\Phi_{12}^a &= (\Phi_{ab}^a + e^{i\frac{\pi}{3}}\Phi_{ac}^a + e^{i\frac{2\pi}{3}}\Phi_{bc}^a)/\sqrt{3}, \\ \Phi_{13}^a &= (\Phi_{ab}^a + e^{-i\frac{\pi}{3}}\Phi_{ac}^a + e^{-i\frac{2\pi}{3}}\Phi_{bc}^a)/\sqrt{3}, \\ \Phi_{23}^a &= (\Phi_{ab}^a - \Phi_{ac}^a + \Phi_{bc}^a)/\sqrt{3}.\end{aligned}\quad (8)$$

In the strongly gapped case, already for marginally weak long-range interactions (as for $\epsilon = 9$ in Fig. 3), the orbitally antisymmetric configurations are favored energetically over the symmetric ones, (as there is no advantage in kinetic energy for orbitally symmetric states compared to the orbitally asymmetric ones) and the splitting within the lowest-energy triplet increases with increasing interaction strength.

In the limit when long-range repulsion is a dominant factor ($\epsilon \rightarrow 1$), the two-particle GS is orbitally antisymmetric for all system parameters. Also, in the latter

case, the 2ESs are more extended compared to the size of the lowest single-particle orbitals, and, due to the more significant exchange gaps, higher orbital single-particle states are involved in forming the 2ES. Therefore, the 2ES in the case $\Delta_0 = 200$, $\epsilon = 1$ in Fig. 3, is the antisymmetric combination of $(\Psi_a + \Psi_b + \Psi_c)(\tilde{\Psi}_a + \tilde{\Psi}_b + \tilde{\Psi}_c)/3$, where Ψ_a, Ψ_b, Ψ_c denote the mini-valley states of the lowest single-particle triplet as in Eq. (6), and $\tilde{\Psi}_a, \tilde{\Psi}_b, \tilde{\Psi}_c$ the corresponding mini-valley states in the third triplet (see SI section S2 for details about these wave functions). This 2ES state is an inter-mini-valley coherent state (see inset to Fig. 3), where all the mini-valleys of the lowest, and the third triplet are occupied simultaneously (as opposed to the incoherent population of one electron per mini-valley in Eq. (8)). For the first excited state there is a competition between the second orbitally antisymmetric state (as in the case $\Delta_0 = 60$, $\epsilon = 1$ in Fig. 3), or the first orbitally symmetric state (which is the first excited state for $\Delta_0 = 200$, $\epsilon = 1$, in Fig. 3). Implied that, depending on the size of the dot and the magnitude of the gap, the first excited states can be four-fold spin and valley degenerate (if the orbital part is antisymmetric), or manifest spin and valley-split levels (if the orbital wave function is symmetric).

The GS multiplets can be split in a magnetic field, B . The valley g-factor, typically $g_v \gg 1^{25,26,37}$, determines the valley splitting of states by B^{28} . For example, the single-particle mini-valley triplet states in the strongly gapped BLG in Fig. 2, remain degenerate in the regime of weak B . For the 2ESs, the valley polarized states, $T^{\pm z}$ split linearly with the magnetic field strength, as opposed to the inter-valley coherent states, $T^{\pm x}$, for which the opposite g-factors from the two valleys cancel.

Finally, one of the intriguing features of the computed spectra is the appearance of an orbitally symmetric two-

particle GS in a weakly gapped, weakly interacting bilayer. In the latter case, the short-range interaction (generally small compared to the Coulomb interaction and the resulting exchange splitting), determines the form of the GS, and we find that inter-valley scattering at the lattice scale favors the formation of a Cooper-pair-like two-particle state. This agrees with the earlier-discussed³⁴ possibility of a singlet superconductor phase in BLG, which is a consequence of the same effectively attractive inter-valley interactions.

In the limit of strong Coulomb repulsion (small ϵ), independently of the microscopic details or characteristics of the dot confinement, the GS is a four-fold degenerate multiplet where all spin and valley configurations ensure antisymmetry of the total wave function. For the excited states, depending on the dot and the gap size, both orbitally antisymmetric, and orbitally symmetric states can occur, and in Fig. 1 we manifest the ordering of the low-energy states and anticipated splittings in a weak perpendicular magnetic field for typical hBN encapsulated BLG devices ($\epsilon \approx 4^{30,44}$) used in the recent experimental studies of BLG quantum dots^{18,22,36}.

ACKNOWLEDGMENTS

We would like to thank A. Kurzmann, P. Rickhaus, M. Eich, K. Ensslin, T. Ihn, R. Kraft, R. Danneau, C. Stampfer, L. Banszerus, S. Slizovskiy, and B. Altshuler for discussions. We acknowledge funding from the European Graphene Flagship Project, the European Quantum Technology Project 2D-SIPC, the ERC Synergy Grant Hetero2D, EPSRC grants EP/S030719/1 and EP/N010345/1, and the Lloyd Register Foundation Nanotechnology Grant.

-
- ¹ B. Delley and E. F. Steigmeier, *Physical Review B* **47**, 1397 (1993).
- ² L.-W. Wang and A. Zunger, *Physical Review Letters* **73**, 1039 (1994).
- ³ J. Cibert, P. M. Petroff, G. J. Dolan, S. J. Pearton, A. C. Gossard, and J. H. English, *Applied Physics Letters* **49**, 1275 (1986).
- ⁴ A. S. Plaut, H. Lage, P. Grambow, D. Heitmann, K. von Klitzing, and K. Ploog, *Physical Review Letters* **67**, 1642 (1991).
- ⁵ K. Brunner, U. Bockelmann, G. Abstreiter, M. Walther, G. Böhm, G. Tränkle, and G. Weimann, *Physical Review Letters* **69**, 3216 (1992).
- ⁶ C. Sikorski and U. Merkt, *Physical Review Letters* **62**, 2164 (1989).
- ⁷ K. Kash, *Journal of Luminescence* **46**, 69 (1990).
- ⁸ P. M. Petroff and S. P. DenBaars, *Superlattices and Microstructures* **15**, 15 (1994).
- ⁹ D. Loss and D. P. DiVincenzo, *Physical Review A* **57**, 120 (1998).
- ¹⁰ X. Zhang, H.-O. Li, K. Wang, G. Cao, M. Xiao, and G.-P. Guo, *Chinese Physics B* **27**, 020305 (2018).
- ¹¹ K. Wang, H.-O. Li, M. Xiao, G. Cao, and G.-P. Guo, *Chinese Physics B* **27**, 090308 (2018).
- ¹² S. Tarucha, M. Yamamoto, A. Oiwa, B.-S. Choi, and Y. Tokura, in *Principles and Methods of Quantum Information Technologies*, Lecture Notes in Physics, edited by Y. Yamamoto and K. Semba (Springer Japan, Tokyo, 2016) pp. 541–567.
- ¹³ D. Cogan, O. Kenneth, N. H. Lindner, G. Peniakov, C. Hopfmann, D. Dalacu, P. J. Poole, P. Hawrylak, and D. Gershoni, *Physical Review X* **8**, 041050 (2018).
- ¹⁴ R. Hanson, L. P. Kouwenhoven, J. R. Petta, S. Tarucha, and L. M. K. Vandersypen, *Reviews of Modern Physics* **79**, 1217 (2007).
- ¹⁵ D. Pfannkuche and R. R. Gerhardts, *Physical Review B* **44**, 13132 (1991).
- ¹⁶ P. A. Maksym, *Physica B: Condensed Matter* **184**, 385 (1993).
- ¹⁷ E. McCann and V. I. Fal'ko, *Physical Review Letters* **96**, 086805 (2006).
- ¹⁸ M. Eich, R. Pisoni, H. Overweg, A. Kurzmann, Y. Lee,

- P. Rickhaus, T. Ihn, K. Ensslin, F. Herman, M. Sigrist, K. Watanabe, and T. Taniguchi, *Physical Review X* **8**, 031023 (2018).
- ¹⁹ H. Overweg, H. Eggimann, X. Chen, S. Slizovskiy, M. Eich, R. Pisoni, Y. Lee, P. Rickhaus, K. Watanabe, T. Taniguchi, V. Fal'ko, T. Ihn, and K. Ensslin, *Nano Letters* **18**, 553 (2018).
- ²⁰ R. Kraft, I. V. Krainov, V. Gall, A. P. Dmitriev, R. Krupke, I. V. Gornyi, and R. Danneau, *Physical Review Letters* **121**, 257703 (2018).
- ²¹ L. Banszerus, B. Frohn, T. Fabian, S. Somanchi, A. Epping, M. Müller, D. Neumaier, K. Watanabe, T. Taniguchi, F. Libisch, B. Beschoten, F. Hassler, and C. Stampfer, arXiv:1911.13176 [cond-mat] (2019), arXiv:1911.13176 [cond-mat].
- ²² L. Banszerus, S. Möller, E. Icking, K. Watanabe, T. Taniguchi, C. Volk, and C. Stampfer, arXiv:1912.11373 [cond-mat] (2019), arXiv:1912.11373 [cond-mat].
- ²³ A. Varlet, D. Bischoff, P. Simonet, K. Watanabe, T. Taniguchi, T. Ihn, K. Ensslin, M. Mucha-Kruczyński, and V. I. Fal'ko, *Physical Review Letters* **113**, 116602 (2014).
- ²⁴ A. Varlet, M. Mucha-Kruczyński, D. Bischoff, P. Simonet, T. Taniguchi, K. Watanabe, V. Fal'ko, T. Ihn, and K. Ensslin, *Synthetic Metals Reviews of Current Advances in Graphene Science and Technology*, **210**, 19 (2015).
- ²⁵ A. Knothe and V. Fal'ko, *Physical Review B* **98**, 155435 (2018), arXiv:1808.03577.
- ²⁶ Y. Lee, A. Knothe, P. Rickhaus, H. Overweg, M. Eich, A. Kurzmann, T. Taniguchi, K. Watanabe, V. Fal'ko, T. Ihn, and K. Ensslin, arXiv:1911.05968 [cond-mat] (2019), arXiv:1911.05968 [cond-mat].
- ²⁷ C. Moulds, A. Knothe, and V. Fal'ko, *Physical Review B* **101**, 085118 (2020).
- ²⁸ The valley g-factor assumes values of $g_v \sim 100$ in BLG, and therefore exceeds the spin g-factor, $g \sim 2$, by orders of magnitude. Any spin splitting is hence neglected in our discussion (c.f. Refs. [26,27]).
- ²⁹ V. V. Cheianov, I. L. Aleiner, and V. I. Fal'ko, *Physical Review Letters* **109**, 106801 (2012).
- ³⁰ N. S. Rytova, arXiv:1806.00976 [cond-mat] (2018), arXiv:1806.00976 [cond-mat].
- ³¹ L. V. Keldysh, *JETPL* **29**, 658 (1979).
- ³² L. V. Keldysh, *ZhPmR* **29**, 716 (1979).
- ³³ Y. Lemonik, I. L. Aleiner, C. Toke, and V. I. Fal'ko, *Physical Review B* **82**, 201408(R) (2010).
- ³⁴ Y. Lemonik, I. Aleiner, and V. I. Fal'ko, *Physical Review B* **85**, 245451 (2012).
- ³⁵ I. L. Aleiner, D. E. Kharzeev, and A. M. Tsvelik, *Physical Review B* **76**, 195415 (2007).
- ³⁶ M. Eich, R. Pisoni, A. Pally, H. Overweg, A. Kurzmann, Y. Lee, P. Rickhaus, K. Watanabe, T. Taniguchi, K. Ensslin, and T. Ihn, *Nano Letters* **18**, 5042 (2018).
- ³⁷ H. Overweg, A. Knothe, T. Fabian, L. Linhart, P. Rickhaus, L. Wernli, K. Watanabe, T. Taniguchi, D. Sánchez, J. Burgdörfer, F. Libisch, V. I. Fal'ko, K. Ensslin, and T. Ihn, *Physical Review Letters* **121**, 257702 (2018).
- ³⁸ E. McCann, D. S. Abergel, and V. I. Fal'ko, *The European Physical Journal Special Topics* **148**, 91 (2007).
- ³⁹ E. McCann and M. Koshino, *Reports on Progress in Physics* **76**, 056503 (2013).
- ⁴⁰ V. Fock, *Zeitschrift für Physik* **47**, 446 (1928).
- ⁴¹ C. G. Darwin, *Mathematical Proceedings of the Cambridge Philosophical Society* **27**, 86 (1931).
- ⁴² D. Xiao, M.-C. Chang, and Q. Niu, *Reviews of Modern Physics* **82**, 1959 (2010).
- ⁴³ M.-C. Chang and Q. Niu, *Physical Review B* **53**, 7010 (1996).
- ⁴⁴ M. E. Levinshtein, S. L. Rumyantsev, and M. S. Shur, *Properties of Advanced Semiconductor Materials: GaN, AlN, InN, BN, SiC, SiGe* (John Wiley & Sons, 2001).
- ⁴⁵ M. Kharitonov, *Physical Review B* **85**, 155439 (2012).
- ⁴⁶ M. Kharitonov, *Physical Review Letters* **109**, 046803 (2012).
- ⁴⁷ S. Slizovskiy, A. Garcia-Ruiz, N. Drummond, and V. I. Fal'ko, arXiv:1912.10067 [cond-mat] (2019), arXiv:1912.10067 [cond-mat].
- ⁴⁸ Note that the values and the sign of the short-range couplings could be affected further by a more realistic shape of the atomic orbitals or by renormalization³⁴. A positive value of g_{\perp} would invert the order of states within the split valley multiplets.

**SUPPLEMENTARY INFORMATION FOR
"QUARTET STATES IN TWO-ELECTRON
QUANTUM DOTS IN BILAYER GRAPHENE"**

**S1. NUMERICAL DIAGONALISATION OF THE
SINGLE PARTICLE HAMILTONIAN**

We can diagonalize the Hamiltonian, H_{\pm}^0 , in Eq. (5) numerically in different bases of localised states. We choose the eigenstates of the two-dimensional harmonic oscillator (products of wave functions $\psi_n(x) = N_n e^{-\frac{1}{2}(\alpha x)^2} \mathcal{H}_n(\alpha x)$, where $N_n = \sqrt{\frac{\alpha}{\sqrt{\pi} 2^n n!}}$ is the normalization constant and α is a scaling factor of unit length⁻¹; we choose α adapted to the potential $U(x)$ obtained from the fit of a parabolic potential to the bottom of U). The basis states are then given by

$$\psi_{\eta\mu,1} \begin{pmatrix} \psi_{\eta}(x)\psi_{\mu}(y) \\ 0 \\ 0 \\ 0 \end{pmatrix}, \psi_{\eta\mu,2} \begin{pmatrix} 0 \\ \psi_{\eta}(x)\psi_{\mu}(y) \\ 0 \\ 0 \end{pmatrix},$$

$$\psi_{\eta\mu,3} \begin{pmatrix} 0 \\ 0 \\ \psi_{\eta}(x)\psi_{\mu}(y) \\ 0 \end{pmatrix}, \psi_{\eta\mu,4} \begin{pmatrix} 0 \\ 0 \\ 0 \\ \psi_{\eta}(x)\psi_{\mu}(y) \end{pmatrix}. \quad (\text{S1})$$

Alternatively, we can use the basis of eigenstates of 2D circular polar confinement in polar coordinates $\psi_{nm}(r, \varphi) = \mathcal{R}_{nm}(r) \mathcal{Y}_m(\varphi)$, where

$$\mathcal{R}_{nm}(r) = N_{nm} (\alpha r)^{|m|} \mathcal{L}[n, |m|, \alpha^2 r^2] e^{-\frac{\alpha^2 r^2}{2}},$$

$$\mathcal{Y}_m(\varphi) = e^{im\varphi}, \quad (\text{S2})$$

where $N_{nm} = \alpha \sqrt{\frac{n!}{\pi(n+|m|)!}}$ ensures normalization and \mathcal{L} denotes the associated Laguerre polynomials.

For every set of system parameters we construct the matrix corresponding to Hamiltonian H_{\pm}^0 in the basis given in Eq. (S1) or Eq. (S2) and obtain the energy spectrum by diagonalization. Convergence is reached when the energy levels do not change anymore upon including a higher number of basis states.

S2. SINGLE PARTICLE SPECTRA

In Figs. S1 and S2 we show additional examples of single-particle QD spectra. Figure S1 illustrates the evolution of the single-particle levels as a function of dot size, L , for different values of Δ_0 . Figure S2 depicts in detail the development from a singlet single-particle GS (small Δ_0), which is clearly separated from the higher energy states, to a three-fold degenerate mini-valley GS (for large Δ_0). In Fig. S3 we quantify the splittings of respective multiplets: The upper panel shows how the splitting

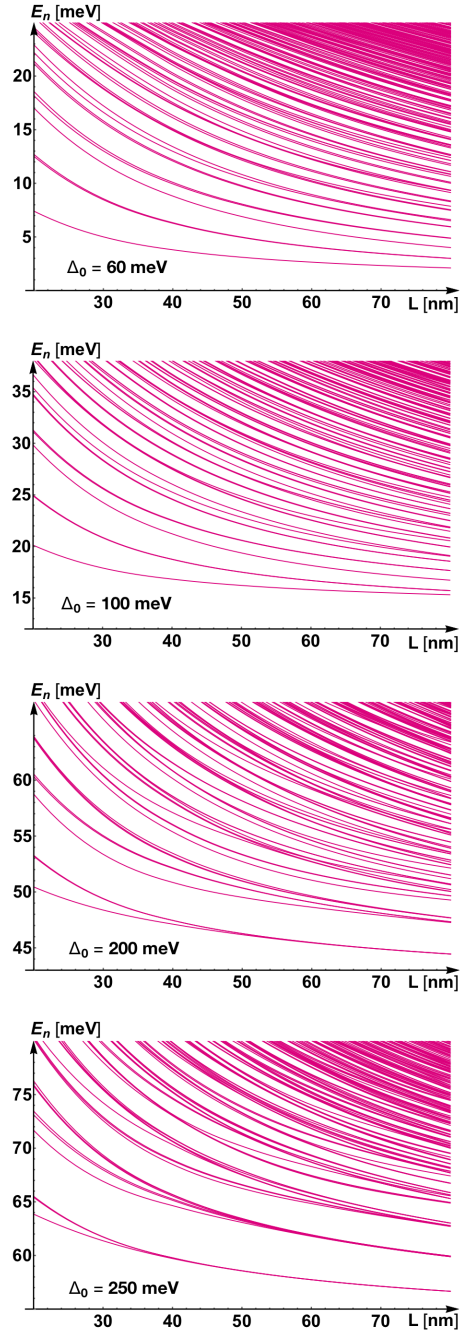


FIG. S1. Single-particle QD spectra for different values of Δ_0 as a function of L .

of the third and the second energy level, $E_3 - E_2$ develops as a function of Δ_0 for different values of L . Since γ_M (as discussed in the main text) is most substantial for small gaps, these two levels split the strongest for small Δ_0 and small dots. Therefore, the splitting decreases with increasing Δ_0 and increasing L . Further, we investigate the splitting of the first and the second energy level, $E_2 - E_1$, as a function of Δ_0 for different values of L (lower panel).

The regime in which the levels of the spectra are each threefold degenerate (corresponding to the three mini-

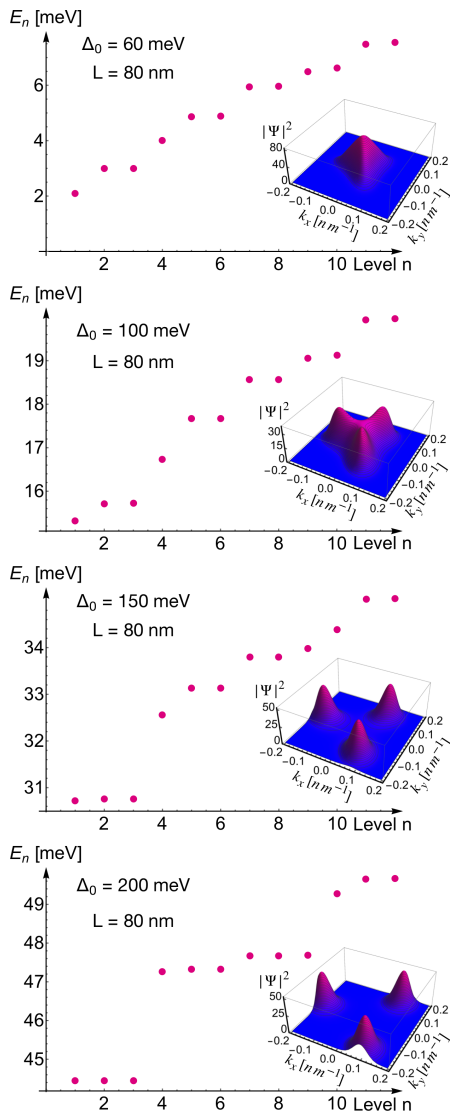


FIG. S2. QD energy spectra for $L = 80$ nm and different Δ_0 . The insets show the probability distribution $|\Psi|^2$ in valley K^- for the lowest level $n = 1$.

valleys around each valley) is realized for large dots and large gaps. In this case, the minivalleys around each of BLG's valleys is sufficiently developed and separated in momentum space to approximately represent a good quantum number. We can hence express the single-particle dot levels in a minivalley basis, where a, b, c label the three minivalleys and $\Psi_{a,b,c}$ denotes the minivalley states of the lowest single-particle triplet, while $\tilde{\Psi}_{a,b,c}$ and $\bar{\Psi}_{a,b,c}$ refer to those of the second and third triplet respectively. The change of basis is illustrated in Fig. S5 where we show the probability distributions of all the mini-valley states both in momentum space and in real space. For comparison, in Fig. S4, we show equally the momentum space and real space distributions of the corresponding nine lowest dot states, $n = 1, \dots, 9$ in the level basis Ψ_n .

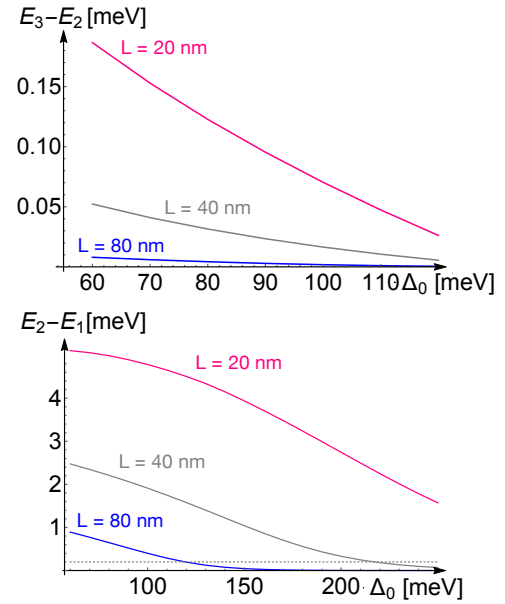


FIG. S3. Properties of the spectra of symmetric QDs in gapped BLG. Upper panel: distance between the third and second level, $E_3 - E_2$, as a function of Δ_0 for different L . Lower panel: distance between the second and first level, $E_2 - E_1$, as a function of Δ_0 for different L .

Single-particle wave functions in the level basis

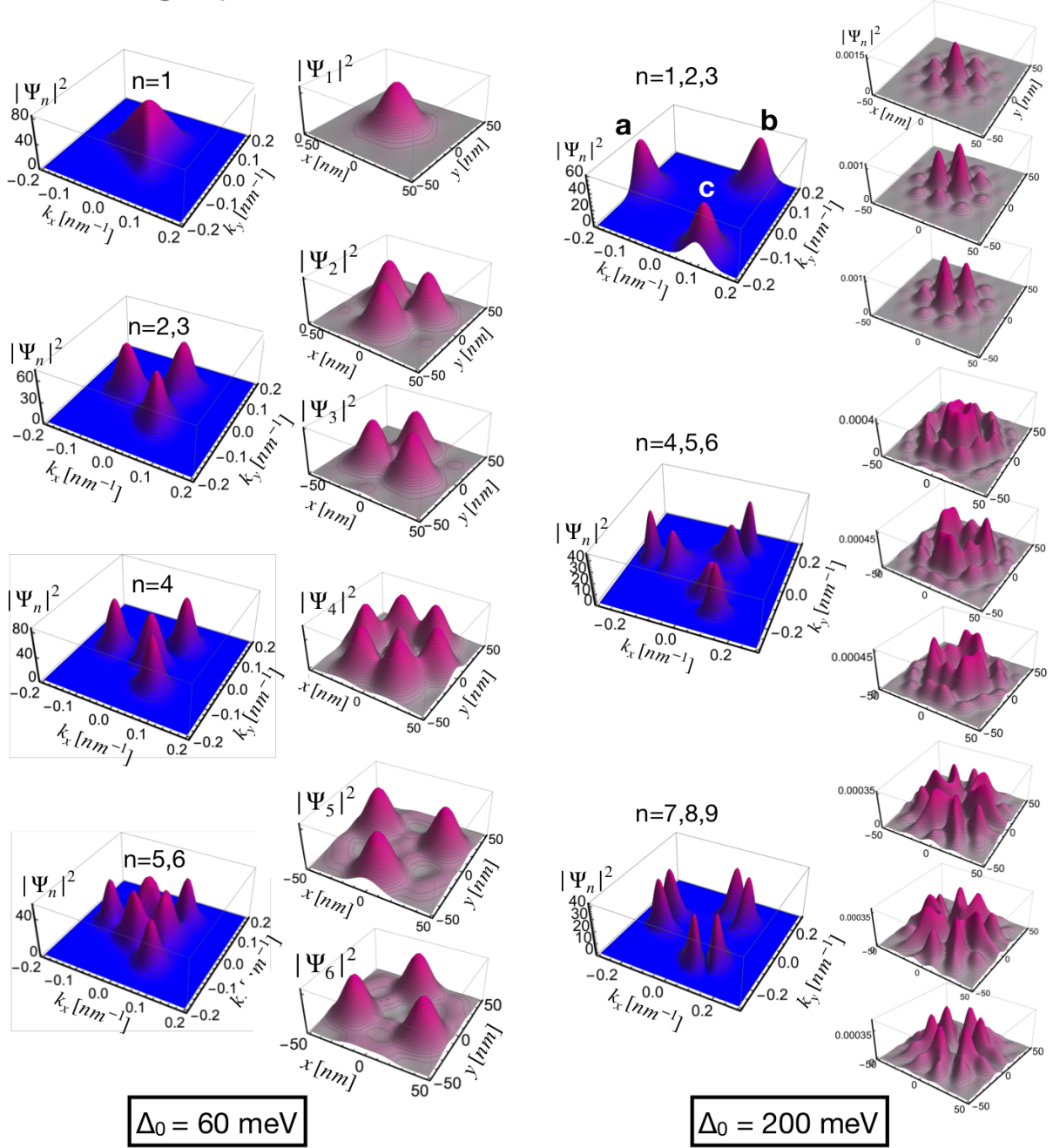


FIG. S4. Momentum space and real space probability distributions for the lowest six ($\Delta_0 = 60$ meV, left), or lowest nine ($\Delta_0 = 200$ meV, right) dot levels for a dot with $L=80$ nm, $\Delta_0 = 200$ meV. These are the states used for the construction of the 2ES.

Single-particle wave functions in the mini-valley basis

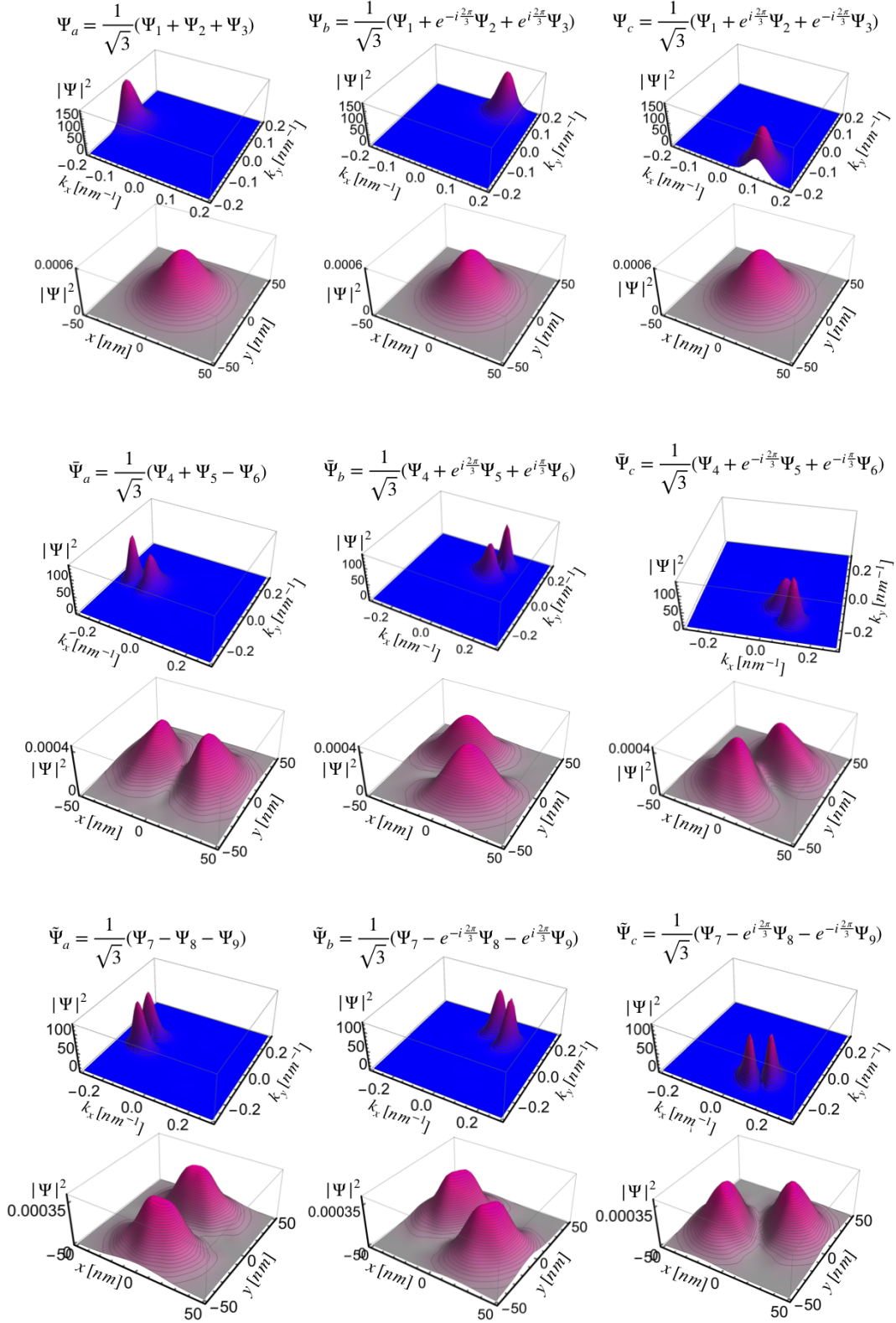


FIG. S5. Transformation from the level basis, Ψ_n , to the basis of mini-valley states, labelled by a, b, c in a strongly gapped BLG QD. We illustrate the probability distributions in momentum space (top rows) and in real space (bottom space) for a dot with $L=80$ nm, $\Delta_0 = 200$ meV.

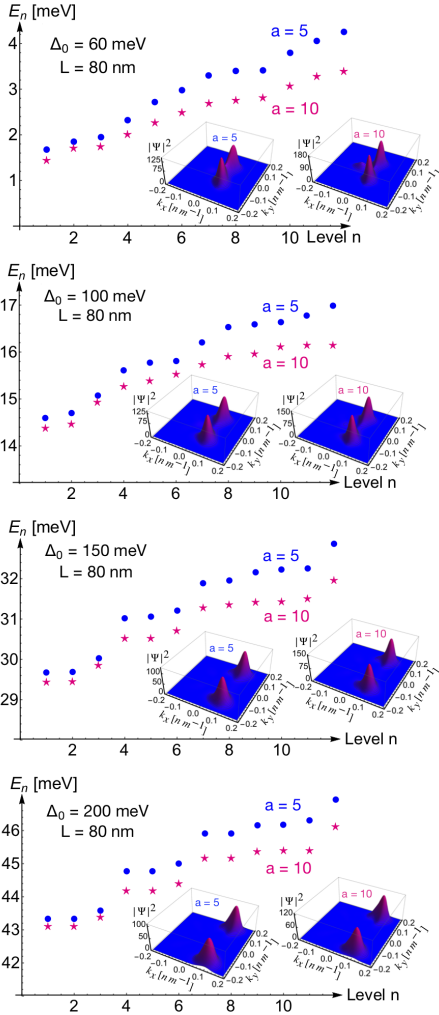


FIG. S6. BLG QD spectra for elliptical QDs with $a = 5$ (blue circles) or $a = 10$ (magenta stars) for $L = 80$ nm and different Δ_0 . The insets show the probability distribution $|\Psi|^2$ in valley K^- for the wave functions of the lowest level $n = 1$, respectively.

Furthermore, we mention the generalization of the model discussed in the main text, when the dot confinement is elliptical with confining potential and gap of the form

$$U(x, y) = \frac{U_0}{\cosh \frac{\sqrt{x^2 + \frac{y^2}{a}}}{L}}, \quad \Delta(x, y) = \Delta_0 - \frac{\beta \Delta_0}{\cosh \frac{\sqrt{x^2 + \frac{y^2}{a}}}{L}}. \quad (\text{S3})$$

The types of confinement described range from the familiar circular symmetric confinement (for $a = 1$) or a potential of elliptical shape (elongated along the y -direction for $a > 1$). Examples for single-particle spectra of elliptical QDs are depicted in Fig. S6.

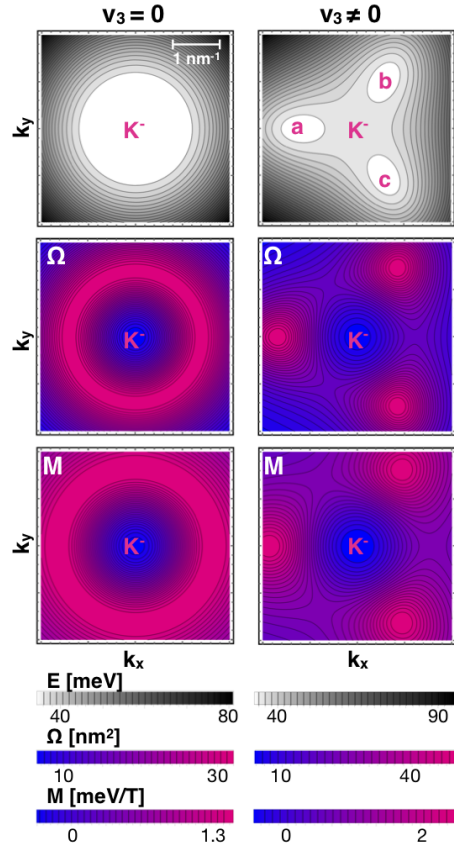


FIG. S7. Electronic structure of homogeneous gapped BLG in the absence of confinement with or without trigonal warping effects (left column, $v_3 \equiv 0$, or right column, $v_3 = 0.12v$). Top panels: electron dispersion of the lowest conduction band. Centre and bottom panels: Berry curvature, $\Omega(\mathbf{k})$, and orbital magnetic moment, $\mathbf{M}(\mathbf{k})$, computed numerically for the lowest conduction band and $\Delta = 70$ meV. In the absence of v_3 the electronic structure has rotational symmetry around the K point, while the trigonally warped structure exhibits three minivalleys in the dispersion (labelled a, b, and c), or three peaks in Ω and M , respectively, around each K point. In the K^+ valley, the structures in momentum space are rotated by π and both, Ω and M , carry opposite sign in the opposite valley.

S3. INFLUENCE OF TRIGONAL WARPING ON DISPERSION AND BERRY CURVATURE

From the Bloch functions of BLG, we obtain the corresponding Berry curvature, $\Omega(\mathbf{k})$, and orbital magnetic moment, $\mathbf{M}(\mathbf{k}) = M(\mathbf{k})\mathbf{e}_z$, as^{42,43}

$$\begin{aligned} \Omega &= i \langle \nabla_{\mathbf{k}} \Phi(\mathbf{k}) | \times | \nabla_{\mathbf{k}} \Phi(\mathbf{k}) \rangle \cdot \mathbf{e}_z, \\ M &= -i \frac{e}{2\hbar} \langle \nabla_{\mathbf{k}} \Phi(\mathbf{k}) | \times [\epsilon(\mathbf{k}) - H(\mathbf{k})] | \nabla_{\mathbf{k}} \Phi(\mathbf{k}) \rangle \cdot \mathbf{e}_z, \end{aligned} \quad (\text{S4})$$

where, $\nabla_{\mathbf{k}} = (\partial_{k_x}, \partial_{k_y})$, " \times " is the cross product, and $\epsilon(\mathbf{k})$ is the band energy. Both quantities, Ω and M , inherit the threefold rotational symmetry of the trigonally warped bands: M and Ω develop non-zero peaks

around the positions of the minivalleys in momentum space, where both, Ω and M , carry opposite sign in the opposite valley. Note that the Berry curvature and the orbital magnetic moment are closely related quantities. In fact, within the two-band model of BLG^{17,38} with $v_3 \rightarrow 0$?, for which $\epsilon(\mathbf{k}) = \sqrt{(\frac{\hbar^2 k^2}{2m})^2 + (\frac{\Delta}{2})^2}$ with $m \approx \frac{\gamma_1}{2v^2} \approx 0.032m_e$ being the effective mass of electrons in BLG, they are directly proportional: $\Omega \approx -\xi \frac{\hbar^2}{2m} \frac{\hbar^2 k^2}{2m} \frac{\Delta}{\epsilon(\mathbf{k})^3}$ and $M \approx -\epsilon(\mathbf{k}) \frac{e}{\hbar} \Omega = \xi \frac{e\hbar}{2m} \frac{\hbar^2 k^2}{2m} \frac{\Delta}{\epsilon(\mathbf{k})^2}$, where $\xi = \pm 1$ labels the two different valleys.

We comment on how trigonal warping, induced by v_3 , breaks continuous rotational symmetry and reduces the symmetry of the dispersion (and, consequently, of the Berry curvature and the orbital magnetic moment) to C_3 . We compare the quantities computed without trigonal warping ($v_3 \equiv 0$) and with trigonal warping ($v_3 \neq 0$) in Fig. S7. To illustrate the effect of the symmetry breaking on the BLG QD spectra and states we show both examples, in the absence and in the presence of trigonal warping, in Figs. S8 and S9, respectively.

In the absence of any symmetry breaking, electrons subject to harmonic circularly isotropic confinement without a magnetic field exhibit quantization into discrete Fock-Darwin energy levels^{40,41},

$$E_{l,m} = (2l + |m| + 1)\hbar\omega_0, \quad (\text{S5})$$

with a characteristic frequency ω_0 and characterised by two quantum numbers, $l \in \mathbb{N}^0$ (radial quantum number), and $m \in \mathbb{Z}$ (angular momentum quantum number).

To demonstrate the effect of the additional orbital angular momentum due to the non-trivial Berry curvature of the states in gapped BLG, it is instructive to consider in some detail the system in the absence of trigonal warping, *i.e.*, for $v_3 \equiv 0$. In this case, when both the confinement and the dispersion exhibit rotational symmetry (see top left panel of Fig. S7), the additional angular momentum due to the Berry curvature represents the only perturbation to the usual Fock-Darwin levels as given in Eq. S5.

In Fig. S8 we show an example of a spectrum for circular confinement in gapped BLG if trigonal warping is neglected for $\Delta_0 = 100$ meV and $L = 80$ nm. We show the probability density for the wave functions, $|\Psi|^2$ in valley K^- and indicate for each level the value of the m quantum number of this state. This spectrum has been calculated for the K^- valley, an equivalent picture is obtained for the K^+ valley with signs of each m reversed. We hence find degeneracy between states with $(K = +1, m)$ and $(K = -1, -m)$. The m quantum number is still close to the integer values prescribed by the Fock-Darwin states with small perturbations due to additional effects by the additional orbital angular momentum influencing the angular momentum of the states. Furthermore, we see from Fig. S8 that, while the spectrum and the wave functions retain some of the properties of the Fock-Darwin levels in zero magnetic field, all

degeneracies between levels with different m in one valley are lifted. Previously exactly degenerate levels with quantum numbers $\pm|m|$ are split apart slightly due to coupling between the orbital magnetic moment, Ω , and the angular momentum \mathbf{L}_z of the form $\Omega \cdot \mathbf{L}_z$. The splitting of these pairs increases with increasing $|m|$. In cases where the previously degenerate state carries a different quantum number m (*i.e.* the triplet $\{l = 1, m = 0\}$, $\{l = 0, m = \pm 2\}$) it is split apart even more strongly from its previously degenerate partners. Due to the different distribution of the wavefunctions in momentum space, states with different $|m|$ pick up different amounts of Berry curvature and therefore carry different orbital magnetic moment. These splittings can be found to be directly proportional to the difference in Berry curvature of states with different $|m|$.

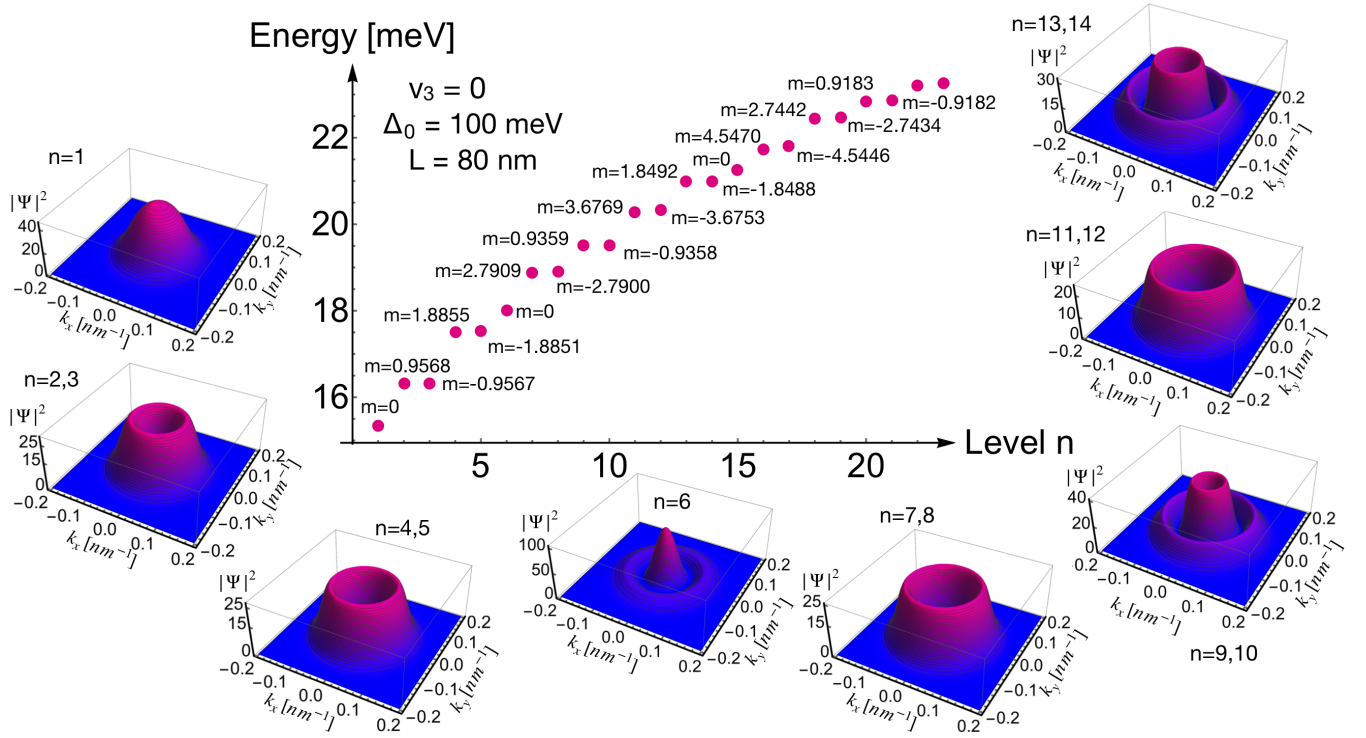


FIG. S8. Energy Levels and wave functions of a circular isotropic BLGQD in the when neglecting trigonal warping for $\Delta_0 = 100$ meV and $L = 80$ nm. For each level, we show the corresponding m quantum number and the probability distribution in momentum space for the wave function on the second lattice atom, $|\Psi|^2$ in valley K^- . This plot is for the K^- valley, in the K^+ valley the picture is identical with the sign of m in each level is reversed and the wave functions are rotated by π .

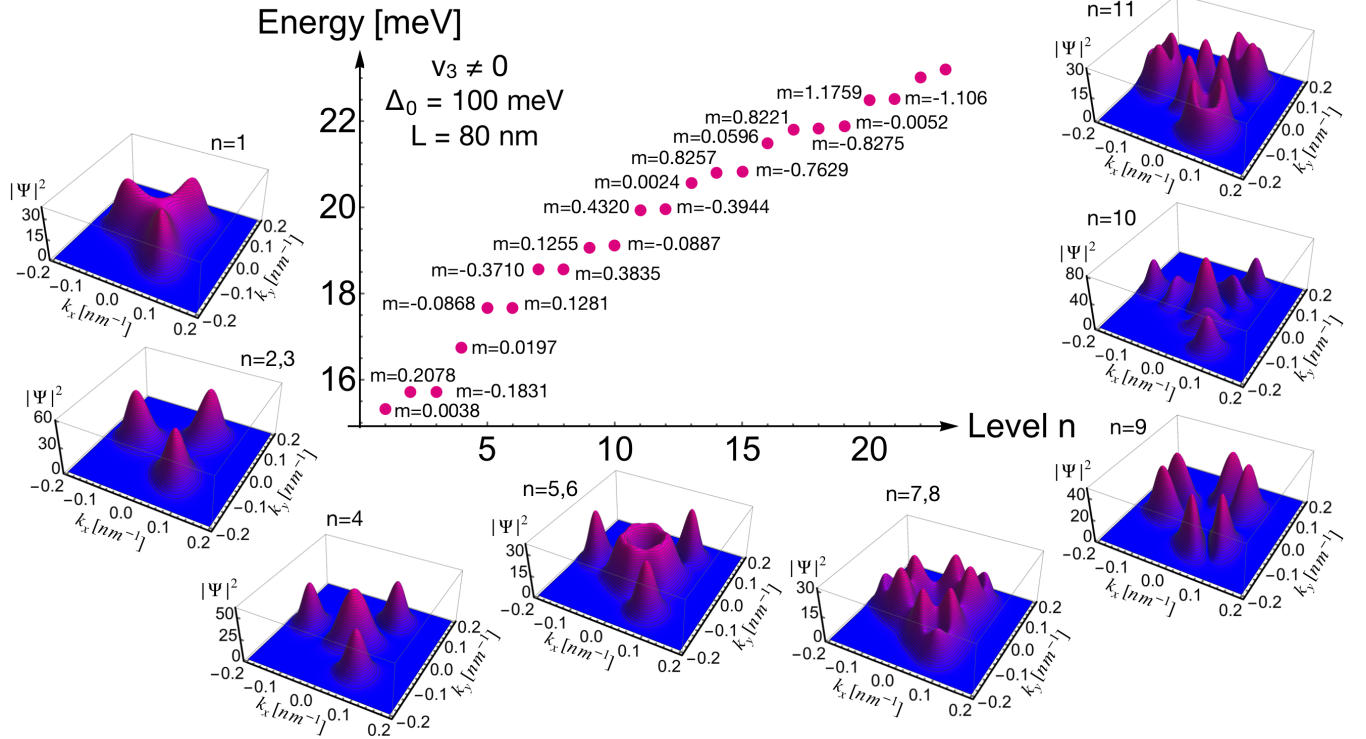


FIG. S9. Same as Fig. S8 for the case when trigonal warping is taken into account.

If $v_3 \neq 0$ is taken into account, the BLG dispersion acquires the trigonally warped dispersion shown in the top right panel of Fig. S7. Therefore, in this case, rotational symmetry is broken even in the presence of rotationally symmetric confinement. In Fig. S9 we demonstrate the effect of trigonal warping on the energy levels, the characterising quantum numbers m , and the corresponding wave functions. Degeneracies are lifted, now due to both, Berry curvature effects and breaking of rotational symmetry. The wave functions exhibit a complex pattern with modes emerging in each mini-valley, separately. As a consequence, the m -values do no longer resemble the integer values of the Fock-Darwin levels.

S4. COUPLING TO AN ELECTRIC FIELD AND OPTICAL TRANSITION MATRIX ELEMENTS

The lowest order term describing coupling between the electrons in BLG and the electromagnetic field (introduced via Peierl's substitution) for small momenta \mathbf{p} is given by[?] ?

$$H_{e-em}^{\pm} = \mathbf{A} \cdot \mathbf{j}^{\pm}, \quad (\text{S6})$$

with the current operator

$$\mathbf{j}^{\pm} = -e \frac{\partial H_{\pm}^0(\mathbf{p})}{\partial \mathbf{p}}. \quad (\text{S7})$$

The incoming light is described by an electric field (neglecting the momentum of the photon compared to that of the electronic states), $\mathbf{E}_{\omega} = \mathbf{E}_{\omega} e^{-i\omega t}$. Using Maxwell's equations, $\mathbf{E} = -\frac{\partial \mathbf{A}}{\partial t}$ (for the transverse field modes which couple to the electronic current), we can write

$$\mathbf{A} = \frac{1}{i\omega} \mathbf{E}_{\omega} e^{-i\omega t}. \quad (\text{S8})$$

We use the numerical wave functions of the electrons in the BLGQD to calculate the matrix elements that determine the rules for transitions between the QD levels. Transitions are induced by absorption of right (\odot) and left-handed (\ominus) circularly polarized light $\mathbf{E}_{\omega} = E_{\omega} \boldsymbol{\ell}_{\odot/\ominus}$, where $\boldsymbol{\ell}_{\odot/\ominus} = \frac{1}{\sqrt{2}}(\mathbf{e}_x \mp \mathbf{e}_y)$, and $\mathbf{e}_{x/y}$ denote unit vectors. We choose the examples $\Delta_0 = 60$, $\Delta_0 = 100$, and $\Delta_0 = 200$ meV to illustrate the optical absorption spectra in Fig. S10. The values for the transition matrix elements in the K^+ valley,

$$t_{n',n}^+ = \langle n' | H_{e-em, \ell_{\odot/\ominus}}^+ | n \rangle, \quad (\text{S9})$$

for different combinations of initial states n and final states n' are summarized in tables S10, S11, S12, respectively, in units of $\frac{meV}{E_{\omega}[mV/nm]/\hbar\omega[meV]}$.

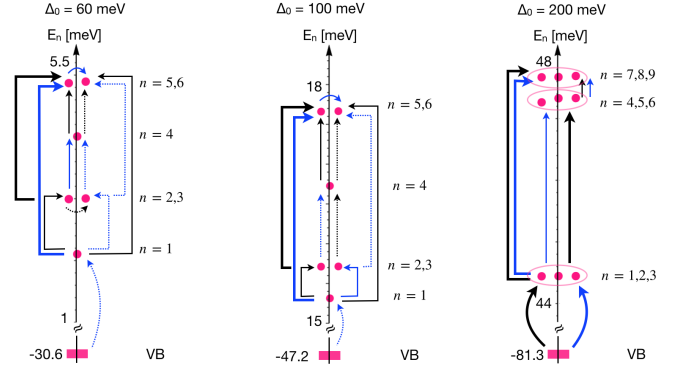


FIG. S10. Channels for optical absorption of right (ℓ_{\odot} , blue arrows) and left-handed (ℓ_{\ominus} , black arrows) circularly polarized light in the K^+ valley. Different arrows indicate different strengths of the transitions, quantified by the transition matrix elements $t_{n',n}^+$: thick line: $t_{n',n}^+ > 1$, thin line: $0.1 < t_{n',n}^+ < 1$, dotted line: $0 < t_{n',n}^+ < 0.1$ (in units of $\frac{meV}{E_{\omega}[mV/nm]/\hbar\omega[meV]}$).

S5. NUMERICAL DIAGONALISATION OF THE TWO-PARTICLE HAMILTONIAN

We use the confined single-particle wave functions of the n th dot level $\Psi_n(\mathbf{r}) = \sum_{(\eta,\mu)} a_{(\eta,\mu)n} \varphi_\eta(x) \varphi_\mu(y)$ from the numerics in the basis of HO eigenfunctions. This allows us to compute the matrix element of the SU(4)-symmetric Coulomb interaction as

$$\begin{aligned}
 V_{n_1, n_2}^{n_3, n_4} &= \iint d\mathbf{r}_1 d\mathbf{r}_2 \Psi_{n_1}(\mathbf{r}_1)^* \Psi_{n_2}(\mathbf{r}_1) V(\mathbf{r}_1 - \mathbf{r}_2) \Psi_{n_3}(\mathbf{r}_2)^* \Psi_{n_4}(\mathbf{r}_2) \\
 &= \int d\mathbf{q} V(\mathbf{q}) \sum_{(\eta,\mu)_{n_1, 2, 3, 4}} a_{(\eta,\mu)_{n_1}}^* a_{(\eta,\mu)_{n_2}} a_{(\eta,\mu)_{n_3}}^* a_{(\eta,\mu)_{n_4}} \\
 &\quad \underbrace{\int dx_1 \varphi_{\eta_1}(x_1) \varphi_{\eta_2}(x_1) e^{iq_x x_1}}_{F_{\eta_1, \eta_2}(q_x)} \underbrace{\int dy_1 \varphi_{\mu_1}(y_1) \varphi_{\mu_2}(y_1) e^{iq_y y_1}}_{F_{\mu_1, \mu_2}(q_y)} \underbrace{\int dx_2 \varphi_{\eta_3}(x_2) \varphi_{\eta_4}(x_2) e^{-iq_x x_2}}_{F_{\eta_3, \eta_4}(-q_x)} \underbrace{\int dy_2 \varphi_{\mu_3}(y_2) \varphi_{\mu_4}(y_2) e^{-iq_y y_2}}_{F_{\mu_3, \mu_4}(-q_y)} \\
 &= \int d\mathbf{q} V(\mathbf{q}) \sum_{(\eta,\mu)_{n_1, 2, 3, 4}} a_{(\eta,\mu)_{n_1}}^* a_{(\eta,\mu)_{n_2}} a_{(\eta,\mu)_{n_3}}^* a_{(\eta,\mu)_{n_4}} F_{\eta_1, \eta_2}(q_x) F_{\mu_1, \mu_2}(q_y) F_{\eta_3, \eta_4}(-q_x) F_{\mu_3, \mu_4}(-q_y). \tag{S13}
 \end{aligned}$$

Here, we exploited that the plane-wave matrix elements of harmonic oscillator eigenfunctions can be obtained analytically and read

$$F_{\eta_1, \eta_2}(q) = \sqrt{\frac{\eta_2!}{\eta_1!}} \left(\frac{iq}{\sqrt{2}\alpha} \right)^{\eta_1 - \eta_2} e^{-\frac{q^2}{4\alpha^2}} L_{\eta_2}^{\eta_1 - \eta_2} \left[\frac{q^2}{2\alpha^2} \right], \tag{S14}$$

for $\eta_2 \leq \eta_1$ and $F_{\eta_2, \eta_1}(q) = [F_{\eta_1, \eta_2}(-q)]^*$. Further, $L_\eta^\mu(x)$ denotes the generalized Laguerre polynomial.

We chose the interaction kernel $V(\mathbf{q})$ as that of the 2D screened Coulomb interaction in a weakly gapped BLG ,

$$V(\mathbf{q}) = \frac{e^2}{4\pi\epsilon_0\epsilon} \frac{2\pi}{q(1 + qR_\star)}. \tag{S15}$$

The screening length $R_\star = \sqrt{32}\hbar\kappa/\sqrt{\Delta}$ (with polarizability $\kappa^2 = 2me^2/(4\pi\epsilon_0\epsilon\hbar\sqrt{\Delta})^2$) defines the spatial range in which the interaction is a Keldysh potential (for $r < R_\star$), or exhibits $1/r$ behaviour (for $r \gg R_\star$). Among others, R_\star depends on the gap induced in the BLG as well as on the dielectric constant, ϵ , of the encapsulating material. In Fig. S11 we show R_\star for a small gap, $\Delta_0 = 60$ meV, and a large gap, $\Delta_0 = 200$ meV, as a function of ϵ . In this figure, we also compare the screening length to the lengthscale of confinement by the QD, which we define as the width of the probability distributions of the confined wave functions.

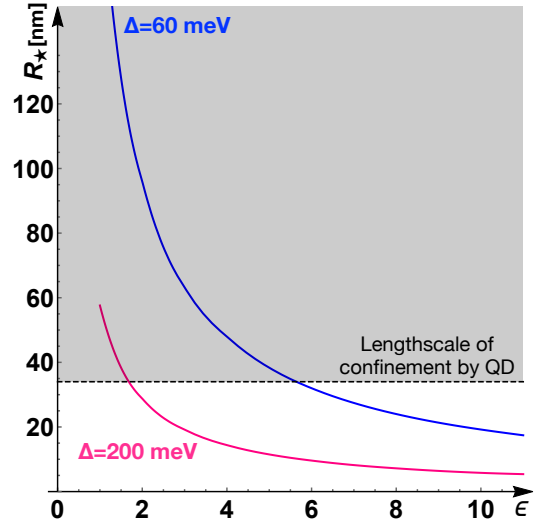


FIG. S11. Screening length, R_\star , for a small gap, $\Delta_0 = 60$ meV, and a large gap, $\Delta_0 = 200$ meV, as a function of ϵ . The dashed line compares to lengthscale of confinement by the QD, obtained from the width of the probability distributions of the confined wave functions.

S6. ESTIMATION OF SHORT-RANGE COUPLINGS

To estimate the contribution of the short range symmetry breaking interaction we start from the form³³⁻³⁵,

$$H_{SR} = \frac{1}{2} \iint d^2\mathbf{r}^2 \sum_{ij} g_{ij} [\Upsilon^\dagger(\mathbf{r}) \sigma_i \tau_j \Upsilon(\mathbf{r})]^2, \tag{S16}$$

where σ_i (τ_i) are the Pauli matrices acting in sub-layer (valley) space. The state Υ comprises the low-energy states on the non-dimer sites A, B' of the BLG lattice assembled in the spinor $\Upsilon = \{\psi_A^K, \psi_{B'}^K, \psi_{B'}^{K'}, -\psi_A^{K'}\}$.

Writing the Hamiltonian of Eq. S16 in matrix form,

$$H_{SR} = \frac{1}{2} \begin{pmatrix} H_{K^+K^+} & H_{K^+K^-} & H_{K^-K^+} & H_{K^-K^-} \\ H_{K^+K^+} & H_{K^+K^-} & H_{K^+K^-} & H_{K^-K^-} \\ H_{K^+K^+} & H_{K^+K^-} & H_{K^-K^+} & H_{K^-K^-} \\ H_{K^+K^+} & H_{K^+K^-} & H_{K^-K^+} & H_{K^-K^-} \end{pmatrix}, \quad (\text{S17})$$

we use the envelope wave functions Ψ of the lowest single-particle dot level at $\Delta_0 = 60$ meV ($\Delta_0 = 200$ meV) and $L = 80$ nm to compute the prefactors numerically. When evaluating the prefactors for the lowest symmetric dot

state

$$W = W_{11,11} = \frac{1}{2} \int d\mathbf{r} \Phi^{s*}_{11}(\mathbf{r}) \Phi_{11}^s(\mathbf{r}), \quad (\text{S18})$$

due to layer polarization in BLG with an external displacement field, we find non-zero matrix elements with weights

$$\begin{aligned} W &= \iint d\mathbf{r} [\Psi_{K^+}^{B'}(\mathbf{r})]^* \Psi_{K^+}^{B'}(\mathbf{r}) [\Psi_{K^+}^{B'}(\mathbf{r})]^* \Psi_{K^+}^{B'}(\mathbf{r}) \\ &= \iint d\mathbf{r} [\Psi_{K^+}^{B'}(\mathbf{r})]^* \Psi_{K^+}^{B'}(\mathbf{r}) [\Psi_{K^-}^{B'}(\mathbf{r})]^* \Psi_{K^-}^{B'}(\mathbf{r}) \\ &= \iint d\mathbf{r} [\Psi_{K^-}^{B'}(\mathbf{r})]^* \Psi_{K^+}^{B'}(\mathbf{r}) [\Psi_{K^+}^{B'}(\mathbf{r})]^* \Psi_{K^-}^{B'}(\mathbf{r}) \\ &= \iint d\mathbf{r} [\Psi_{K^-}^{B'}(\mathbf{r})]^* \Psi_{K^+}^{B'}(\mathbf{r}) [\Psi_{K^-}^{B'}(\mathbf{r})]^* \Psi_{K^+}^{B'}(\mathbf{r}) \\ &= \frac{4.3 * 10^{-4}}{nm^2} \left(\frac{3.7 * 10^{-4}}{nm^2} \right), \end{aligned} \quad (\text{S19})$$

as well as their complex conjugates, while all other matrix elements in Eq. (S17) vanish. Hence, the Hamiltonian in Eq. (S17) reduces to

$$H_{SR} = W \begin{pmatrix} g_{z0} + g_{0z} + g_{zz} & 0 & 0 & 0 \\ 0 & -g_{z0} - g_{0z} + g_{zz} & g_{xx} + g_{yy} + g_{xy} + g_{yx} & 0 \\ 0 & g_{xx} + g_{yy} + g_{xy} + g_{yx} & -g_{z0} - g_{0z} + g_{zz} & 0 \\ 0 & 0 & 0 & g_{z0} + g_{0z} + g_{zz} \end{pmatrix}. \quad (\text{S20})$$

We estimate corresponding couplings g_{ij} in a simple tight-binding model for graphene's p_z -orbital electrons⁷. Writing the Bloch part of the wave function as $v(\mathbf{r}) = (u_{K^+}^A(\mathbf{r}), u_{K^+}^{B'}(\mathbf{r}), u_{K^-}^{B'}(\mathbf{r}), -u_{K^-}^A(\mathbf{r}))^T$, the couplings read^{33-35,45}

$$g_{ij} \propto \int d^3\mathbf{r}_1 \int_{\text{unit cell}} d^3\mathbf{r}_2 \frac{\rho_{ij}(\mathbf{r}_1) \rho_{ij}(\mathbf{r}_2)}{A|\mathbf{r}_1 - \mathbf{r}_2|}, \quad (\text{S21})$$

where $A = |\mathbf{a}_1 \times \mathbf{a}_2|$ is the unit cell area of graphene computed from graphene's real space lattice vectors $\mathbf{a}_1, \mathbf{a}_2$, and

$$\rho_{ij}(\mathbf{r}) = \frac{1}{2} v^\dagger(\mathbf{r}) \sigma_i \tau_j v(\mathbf{r}). \quad (\text{S22})$$

For the Bloch functions we choose the form

$$\begin{aligned} u_{K^\pm}^{A1/B2}(\mathbf{r}) &= \frac{\sqrt{A}}{\sqrt{N}} \sum_{\mathbf{R}_i} e^{i\mathbf{K} \pm \mathbf{R}_i} \varphi_{210}(\mathbf{r} - \mathbf{R}_i), \\ \varphi_{210}(\mathbf{r}) &= \frac{N}{\sqrt{a_0^3}} P(r) Y_0^1(\theta, \phi), \end{aligned} \quad (\text{S23})$$

ensuring normalization⁷ $\int_{\text{unit cell}} u^*(\mathbf{r}) u(\mathbf{r}) d^3\mathbf{r} = A$. In the equations above, $N = \frac{2Z}{\sqrt{32}} \sqrt{\frac{Z^3}{3}}$, $P(r) = \frac{r}{a_0} e^{-\frac{r}{2} \frac{r}{a_0}}$, and Y_m^l denote the spherical harmonics of graphene's $2p_z$ state. Further, Z is the atomic number, $a_0 = \frac{4\pi\epsilon_0\hbar}{m_e e^2 Z}$ is the Bohr radius, and $\{\mathbf{R}_i\}$ denote the lattice points of the sublattice the wave function is residing on. We distinguish between the different scattering processes,

$$\begin{aligned}
M_{intra\ same} &= \frac{e^2}{4\pi\epsilon_C\epsilon_0} \int d\mathbf{r}_1^3 \int_{unit\ cell} d\mathbf{r}_2^3 \frac{1}{4A|\mathbf{r}_2 - \mathbf{r}_1|} (u_{K^+}^{A_1})^*(\mathbf{r}_1)(u_{K^+}^{A_1})^*(\mathbf{r}_2)u_{K^+}^{A_1}(\mathbf{r}_1)u_{K^+}^{A_1}(\mathbf{r}_2) \\
&= \frac{e^2}{4\pi\epsilon_C\epsilon_0} \int d\mathbf{r}_1^3 \int_{unit\ cell} d\mathbf{r}_2^3 \frac{1}{4A|\mathbf{r}_2 - \mathbf{r}_1|} (u_{K^-}^{A_1})^*(\mathbf{r}_1)(u_{K^-}^{A_1})^*(\mathbf{r}_2)u_{K^-}^{A_1}(\mathbf{r}_1)u_{K^-}^{A_1}(\mathbf{r}_2) \\
&= \frac{e^2}{4\pi\epsilon_C\epsilon_0} \int d\mathbf{r}_1^3 \int_{unit\ cell} d\mathbf{r}_2^3 \frac{1}{4A|\mathbf{r}_2 - \mathbf{r}_1|} (u_{K^+}^{B_2})^*(\mathbf{r}_1)(u_{K^+}^{B_2})^*(\mathbf{r}_2)u_{K^+}^{B_2}(\mathbf{r}_1)u_{K^+}^{B_2}(\mathbf{r}_2) \\
&= \frac{e^2}{4\pi\epsilon_C\epsilon_0} \int d\mathbf{r}_1^3 \int_{unit\ cell} d\mathbf{r}_2^3 \frac{1}{4A|\mathbf{r}_2 - \mathbf{r}_1|} (u_{K^-}^{B_2})^*(\mathbf{r}_1)(u_{K^-}^{B_2})^*(\mathbf{r}_2)u_{K^-}^{B_2}(\mathbf{r}_1)u_{K^-}^{B_2}(\mathbf{r}_2) \\
M_{intra\ diff} &= \frac{e^2}{4\pi\epsilon_C\epsilon_0} \int d\mathbf{r}_1^3 \int_{unit\ cell} d\mathbf{r}_2^3 \frac{1}{4A|\mathbf{r}_2 - \mathbf{r}_1|} (u_{K^+}^{A_1})^*(\mathbf{r}_1)(u_{K^+}^{B_2})^*(\mathbf{r}_2)u_{K^+}^{A_1}(\mathbf{r}_1)u_{K^+}^{B_2}(\mathbf{r}_2) \\
&= \frac{e^2}{4\pi\epsilon_C\epsilon_0} \int d\mathbf{r}_1^3 \int_{unit\ cell} d\mathbf{r}_2^3 \frac{1}{4A|\mathbf{r}_2 - \mathbf{r}_1|} (u_{K^-}^{A_1})^*(\mathbf{r}_1)(u_{K^-}^{B_2})^*(\mathbf{r}_2)u_{K^-}^{A_1}(\mathbf{r}_1)u_{K^-}^{B_2}(\mathbf{r}_2) \\
&= \frac{e^2}{4\pi\epsilon_C\epsilon_0} \int d\mathbf{r}_1^3 \int_{unit\ cell} d\mathbf{r}_2^3 \frac{1}{4A|\mathbf{r}_2 - \mathbf{r}_1|} (u_{K^+}^{B_2})^*(\mathbf{r}_1)(u_{K^+}^{A_1})^*(\mathbf{r}_2)u_{K^+}^{B_2}(\mathbf{r}_1)u_{K^+}^{A_1}(\mathbf{r}_2) \\
&= \frac{e^2}{4\pi\epsilon_C\epsilon_0} \int d\mathbf{r}_1^3 \int_{unit\ cell} d\mathbf{r}_2^3 \frac{1}{4A|\mathbf{r}_2 - \mathbf{r}_1|} (u_{K^-}^{B_2})^*(\mathbf{r}_1)(u_{K^-}^{A_1})^*(\mathbf{r}_2)u_{K^-}^{B_2}(\mathbf{r}_1)u_{K^-}^{A_1}(\mathbf{r}_2) \\
M_{inter\ same} &= \frac{e^2}{4\pi\epsilon_C\epsilon_0} \int d\mathbf{r}_1^3 \int_{unit\ cell} d\mathbf{r}_2^3 \frac{1}{4A|\mathbf{r}_2 - \mathbf{r}_1|} (u_{K^-}^{A_1})^*(\mathbf{r}_1)(u_{K^+}^{A_1})^*(\mathbf{r}_2)u_{K^+}^{A_1}(\mathbf{r}_1)u_{K^-}^{A_1}(\mathbf{r}_2) \\
&= \frac{e^2}{4\pi\epsilon_C\epsilon_0} \int d\mathbf{r}_1^3 \int_{unit\ cell} d\mathbf{r}_2^3 \frac{1}{4A|\mathbf{r}_2 - \mathbf{r}_1|} (u_{K^+}^{A_1})^*(\mathbf{r}_1)(u_{K^-}^{A_1})^*(\mathbf{r}_2)u_{K^-}^{A_1}(\mathbf{r}_1)u_{K^+}^{A_1}(\mathbf{r}_2) \\
&= \frac{e^2}{4\pi\epsilon_C\epsilon_0} \int d\mathbf{r}_1^3 \int_{unit\ cell} d\mathbf{r}_2^3 \frac{1}{4A|\mathbf{r}_2 - \mathbf{r}_1|} (u_{K^-}^{B_2})^*(\mathbf{r}_1)(u_{K^+}^{B_2})^*(\mathbf{r}_2)u_{K^+}^{B_2}(\mathbf{r}_1)u_{K^-}^{B_2}(\mathbf{r}_2) \\
&= \frac{e^2}{4\pi\epsilon_C\epsilon_0} \int d\mathbf{r}_1^3 \int_{unit\ cell} d\mathbf{r}_2^3 \frac{1}{4A|\mathbf{r}_2 - \mathbf{r}_1|} (u_{K^+}^{B_2})^*(\mathbf{r}_1)(u_{K^-}^{B_2})^*(\mathbf{r}_2)u_{K^-}^{B_2}(\mathbf{r}_1)u_{K^+}^{B_2}(\mathbf{r}_2) \\
M_{inter\ diff} &= \frac{e^2}{4\pi\epsilon_C\epsilon_0} \int d\mathbf{r}_1^3 \int_{unit\ cell} d\mathbf{r}_2^3 \frac{1}{4A|\mathbf{r}_2 - \mathbf{r}_1|} (u_{K^-}^{A_1})^*(\mathbf{r}_1)(u_{K^+}^{B_2})^*(\mathbf{r}_2)u_{K^+}^{A_1}(\mathbf{r}_1)u_{K^-}^{B_2}(\mathbf{r}_2) \\
&= \frac{e^2}{4\pi\epsilon_C\epsilon_0} \int d\mathbf{r}_1^3 \int_{unit\ cell} d\mathbf{r}_2^3 \frac{1}{4A|\mathbf{r}_2 - \mathbf{r}_1|} (u_{K^+}^{A_1})^*(\mathbf{r}_1)(u_{K^-}^{B_2})^*(\mathbf{r}_2)u_{K^-}^{A_1}(\mathbf{r}_1)u_{K^+}^{B_2}(\mathbf{r}_2) \\
&= \frac{e^2}{4\pi\epsilon_C\epsilon_0} \int d\mathbf{r}_1^3 \int_{unit\ cell} d\mathbf{r}_2^3 \frac{1}{4A|\mathbf{r}_2 - \mathbf{r}_1|} (u_{K^-}^{B_2})^*(\mathbf{r}_1)(u_{K^+}^{A_1})^*(\mathbf{r}_2)u_{K^+}^{B_2}(\mathbf{r}_1)u_{K^-}^{A_1}(\mathbf{r}_2) \\
&= \frac{e^2}{4\pi\epsilon_C\epsilon_0} \int d\mathbf{r}_1^3 \int_{unit\ cell} d\mathbf{r}_2^3 \frac{1}{4A|\mathbf{r}_2 - \mathbf{r}_1|} (u_{K^+}^{B_2})^*(\mathbf{r}_1)(u_{K^-}^{A_1})^*(\mathbf{r}_2)u_{K^-}^{B_2}(\mathbf{r}_1)u_{K^+}^{A_1}(\mathbf{r}_2), \tag{S24}
\end{aligned}$$

where "intra/inter" refer to inter- and intra-valley scattering and "same/different" label processes on the same

sublattice or involving different sublattices, respectively. Within a two-centre approximation we can write the real space integral as

$$\begin{aligned}
M &= \frac{e^2}{4\pi\epsilon_C\epsilon_0} \int d\mathbf{r}_1^3 \int_{\text{unit cell}} d\mathbf{r}_2^3 \frac{1}{4A|\mathbf{r}_2 - \mathbf{r}_1|} (u_{K^\pm}^{A_1/B_2})^*(\mathbf{r}_1) (u_{K^\pm}^{A_1/B_2})^*(\mathbf{r}_2) u_{K^\pm}^{A_1/B_2}(\mathbf{r}_1) u_{K^\pm}^{A_1/B_2}(\mathbf{r}_2) \\
&\approx \frac{e^2}{4\pi\epsilon_C\epsilon_0} \frac{A}{4} \sum_{\mathbf{R}} e^{i\Delta\mathbf{K}\cdot\mathbf{R}} \iint d\mathbf{r}_1^3 d\mathbf{r}_2^3 \frac{1}{|\mathbf{r}_2 - \mathbf{r}_1 + \mathbf{R}|} |\varphi_{210}(\mathbf{r}_1)|^2 |\varphi_{210}(\mathbf{r}_2)|^2,
\end{aligned} \tag{S25}$$

where $\mathbf{R} = \mathbf{R}^{(2)} - \mathbf{R}^{(1)}$ connects the centres of the two wave packages.

We evaluate the real-space integral in Eq. (S25) in two steps. For $\mathbf{R} \equiv 0$ we can use the Laplace expansion of the Coulomb interaction,

$$\frac{1}{|\mathbf{r}_2 - \mathbf{r}_1|} = \sum_{l=0}^{\infty} \frac{r_{<}^l}{r_{>}^{l+1}} \sum_{m=-l}^{m=+l} \frac{4\pi}{2l+1} (Y_m^l)^*(\theta_1, \phi_1) Y_m^l(\theta_2, \phi_2), \tag{S26}$$

and the identity

$$\begin{aligned}
&\int \sin\theta d\theta d\phi Y_{m_1}^{l_1}(\theta, \phi) Y_{m_2}^{l_2}(\theta, \phi) Y_{m_3}^{l_3}(\theta, \phi) \\
&= \sqrt{\frac{(2l_1+1)(2l_2+1)(2l_3+1)}{4\pi}} \begin{pmatrix} l_1 & l_2 & l_3 \\ 0 & 0 & 0 \end{pmatrix} \begin{pmatrix} l_1 & l_2 & l_3 \\ m_1 & m_2 & m_3 \end{pmatrix},
\end{aligned} \tag{S27}$$

and the integral above evaluates to

$$\begin{aligned}
\mathcal{M}_0 &= \frac{e^2}{4\pi\epsilon_C\epsilon_0} \frac{A}{4} \iint d\mathbf{r}_1^3 d\mathbf{r}_2^3 \frac{1}{|\mathbf{r}_2 - \mathbf{r}_1|} |\varphi_{210}(\mathbf{r}_1)|^2 |\varphi_{210}(\mathbf{r}_2)|^2 \\
&= \frac{e^2}{4\pi\epsilon_C\epsilon_0 a_0} \frac{A}{4} Z \frac{501}{2560}.
\end{aligned} \tag{S28}$$

In the case $\mathbf{R} \neq 0$ we employ the expansion^{??} for $|\mathbf{r}_2 - \mathbf{r}_1| < R$,

$$\frac{1}{|\mathbf{r}_2 - \mathbf{r}_1 + \mathbf{R}|} = \sum_{l_a, l_b=0}^{\infty} R^{-(l_a+l_b+1)} r_1^{l_a} r_2^{l_b} V_{l_a, l_b}; \tag{S29}$$

where

$$\begin{aligned}
V_{l_a, l_b} &= (4\pi)^{\frac{3}{2}} (-1)^{l_b} \begin{pmatrix} 2(l_a+l_b) \\ 2l_a \end{pmatrix}^{\frac{1}{2}} \frac{1}{\sqrt{(2l_a+1)(2l_b+1)(2(l_a+l_b)+1)}} \\
&\times \sum_{M=-(l_a+l_b)}^{l_a+l_b} (-1)^M Y_{-M}^L(\theta_R, \phi_R) \left(\sum_{m_a=-l_a}^{l_a} \sum_{m_b=-l_b}^{l_b} Y_{m_a}^{l_a}(\theta_1, \phi_1) Y_{m_b}^{l_b}(\theta_2, \phi_2) \langle l_a m_a; l_b m_b | (l_a+l_b) M \rangle \right).
\end{aligned} \tag{S30}$$

This allows us to compute the integral according to

$$\begin{aligned}
\mathcal{M}_{\mathbf{R} \neq 0} &= \frac{e^2}{4\pi\epsilon_C\epsilon_0} \frac{A}{4} \iint d\mathbf{r}_1^3 d\mathbf{r}_2^3 \frac{1}{|\mathbf{r}_2 - \mathbf{r}_1 + \mathbf{R}|} |\Psi_{210}(\mathbf{r}_1)|^2 |\Psi_{210}(\mathbf{r}_2)|^2 \\
&= \frac{e^2}{4\pi\epsilon_C\epsilon_0 a_0} \frac{A}{4} \left[\frac{1}{(R/a_0)} + \frac{2}{25\sqrt{\pi}} \frac{1}{(R/a_0)^3} Y_0^2(\theta_R, \phi_R) \frac{30}{Z^2} \right. \\
&\left. + \frac{4}{125\sqrt{\pi}} \frac{1}{(R/a_0)^5} Y_0^4(\theta_R, \phi_R) \frac{900}{Z^4} \right].
\end{aligned} \tag{S31}$$

Using Eqs. (S28) and (S31) the sum over the vectors

$\{\mathbf{R}\}$ in Eq. (S25) can be carried out numerically.

We calculate the couplings involving the different scattering processes above,

$$\begin{aligned}
g_{0z} &= g_{z0} = 4M_{\text{same}}^{\text{intra}} - 4M_{\text{same}}^{\text{intra}} + 4M_{\text{diff}}^{\text{intra}} - 4M_{\text{diff}}^{\text{intra}} = 0, \\
g_{zz} &= 8M_{\text{same}}^{\text{intra}} - 8M_{\text{diff}}^{\text{intra}}, \\
g_{xx} &= g_{yx} = 4M_{\text{same}}^{\text{inter}} - 4M_{\text{diff}}^{\text{inter}}, \\
g_{yy} &= g_{xy} = 4M_{\text{same}}^{\text{inter}} + 4M_{\text{diff}}^{\text{inter}},
\end{aligned}$$

small gap, weak interaction			
	orbital	spin valley	\mathfrak{E}_{2P}
first excited state	Φ_1^a	S=0 T^{-x}	\mathfrak{E}_1^a
		S=1 $T^{\pm z}$	
		S=1 T^{+x}	
ground state	Φ_1^s	S=1 T^{-x}	$\mathfrak{E}_1^s + W(g_{zz} - 4g_{\perp})$
		S=0 $T^{\pm z}$	$\mathfrak{E}_1^s + Wg_{zz}$
		S=0 T^{+x}	$\mathfrak{E}_1^s + W(g_{zz} + 4g_{\perp})$

Small gap, strong interaction			
	orbital	spin valley	\mathfrak{E}_{2P}
first excited state	Φ_2^a	S=0 T^{-x}	\mathfrak{E}_2^a
		S=1 $T^{\pm z}$	
		S=1 T^{+x}	
ground state	Φ_1^a	S=0 T^{-x}	\mathfrak{E}_1^a
		S=1 $T^{\pm z}$	
		S=1 T^{+x}	

large gap, strong interaction			
	orbital	spin valley	\mathfrak{E}_{2P}
first excited state	Φ_1^s	S=1 T^{-x}	$\mathfrak{E}_1^s + W(g_{zz} - 4g_{\perp})$
		S=0 $T^{\pm z}$	$\mathfrak{E}_1^s + Wg_{zz}$
		S=0 T^{+x}	$\mathfrak{E}_1^s + W(g_{zz} + 4g_{\perp})$
ground state	Φ_1^a	S=0 T^{-x}	\mathfrak{E}_1^a
		S=1 $T^{\pm z}$	
		S=1 T^{+x}	

TABLE I. States structure and total energies of the two-particle states in orbital, spin, and valley space.

where the first line evaluates to zero because of the property $u_{K^+}^*(\mathbf{r}) = u_{K^-}(\mathbf{r})$. Furthermore, we find

$$M_{diff}^{inter} = \sum_{\mathbf{R}} e^{i(\mathbf{K}^+ - \mathbf{K}^-) \cdot (\mathbf{R} + \mathbf{R}_{AB})} \mathcal{M}_{R+R_{AB}} \equiv 0, \quad (\text{S32})$$

when summing numerically over $\mathbf{R} = c_1 \mathbf{a}_1 + c_2 \mathbf{a}_2$, with non-zero integers c_1, c_2 , and extrapolating to infinite lattices. The vector \mathbf{R}_{AB} connects the A and B sublattices on the two different layers. This property restores the symmetry $g_{xx} = g_{yy} = g_{xy} = g_{yx} =: g_{\perp}$. The two remaining nonzero parameters g_{zz} and g_{\perp} read,

$$g_{zz} = 8\mathcal{M}_0 - 8\mathcal{M}_{R_{AB}} + 8 \sum_{\mathbf{R} \neq 0} (\mathcal{M}_{\mathbf{R}} - \mathcal{M}_{\mathbf{R} + \mathbf{R}_{AB}})$$

$$g_{\perp} = 4\mathcal{M}_0 + 4 \sum_{\mathbf{R} \neq 0} e^{i(\mathbf{K}^+ - \mathbf{K}^-) \cdot \mathbf{R}} \mathcal{M}_{\mathbf{R}},$$

which, using $Z=1$ (assuming the inner core electrons of carbon to be fully screened), evaluate to $g_{zz} = 4.04/\epsilon_C$ eVnm² and $g_{\perp} = -0.191/\epsilon_C$ eVnm².

S7. PROPERTIES OF THE LOW-ENERGY TWO-ELECTRON STATES

In table I we summarize the orbital, spin, and valley configuration alongside with the total energy of the GS and first excited state of two interacting electrons in the QD, for the different cases shown in Fig. 3 of the main text.